This is a repository copy of *The Physcomitrella patens chromosome‐scale assembly reveals moss genome structure and evolution*.

White Rose Research Online URL for this paper:
http://eprints.whiterose.ac.uk/125770/

Version: Accepted Version

The P. patens chromosome-scale assembly reveals moss genome structure and evolution.

Daniel Lang[1,2,*], Kristian K. Ullrich[3,4*], Florent Murat[5], Jörg Fuchs[6], Jerry Jenkins[7], Fabian B. Haas[3], Mathieu Piednoel[8], Heidrun Gundlach[40], Michiel Van Bel[9,10], Rabea Meyberg[3], Cristina Vives[11], Jordi Morata[11], Aikaterini Symeonidi[3,12], Manuel Hiss[3], Wellington Muchero[13], Yasuko Kamisugi[14], Omar Saleh[1,15], Guillaume Blanc[16], Eva L. Decker[1], Nico van Gessel[1], Jane Grimwood[17], Richard D. Hayes[18], Sean W. Graham[19], Lee E. Gunter[13], Stuart McDaniel[20], Sebastian N.W. Hoernstein[1], Anders Larsson[21], Fay-Wei Li[22], Pierre-Francois Perroud[3], Jeremy Phillips[18], Priya Ranjan[13], Daniel S. Rokshar[18,23], Carl J. Rothfels[24], Lucas Schneider[3,25], Shengqiang Shu[18], Dennis W. Stevenson[26], Fritz Thümmler[27], Michael Tillich[28], Juan Carlos Villarreal A.[29], Thomas Widiez[30,41,42], Gane Ka-Shu Wong[31,32,33], Ann Wymore[13], Yong Zhang[34], Andreas D. Zimmer[1, 35], Ralph S. Quatrano[36], Klaus F.X. Mayer[39, 40], David Goodstein[18], Josep M. Casacuberta[11], Klaas Vandepoele[9,10], Ralf Reski[1, 37], Andrew C. Cuming[14], Jerry Tuskan[13], Florian Maumus[38], Jérome Salse[5], Jeremy Schmutz[17], Stefan A. Rensing[3,37+]

[1] Plant Biotechnology, Faculty of Biology, Schaenzlestr. 1, University of Freiburg, 79104 Freiburg, Germany

[2] Current: Plant Genome and Systems Biology, Helmholtz Center Munich, 85764 Neuherberg, Germany

[3] Plant Cell Biology, Faculty of Biology, University of Marburg, Marburg, Germany

[4] Current: Max Planck Institute for Evolutionary Biology, August-Thienemann-Straße 2, 24306 Ploen, Germany

[5] INRA UMR 1095 Genetics, Diversity and Ecophysiology of Cereals (GDEC), 5 Chemin de Beaulieu, 63100 Clermont-Ferrand. France

[6] Leibniz Institute of Plant Genetics and Crop Plant Research (IPK), OT Gatersleben, Corrensstrasse 3, D-06466 Stadt Seeland, Germany

[7] HudsonAlpha Institute for Biotechnology, USA

[8] Department of Plant Developmental Biology, Max Planck Institute for Plant Breeding Research, Carl-von-Linné Weg 10, D-50829 Cologne, Germany

[9] Department of Plant Systems Biology, VIB, Technologiepark 927, B-9052 Gent, Belgium

[10] Department of Plant Biotechnology and Bioinformatics, Ghent University, Technologiepark 927, B-9052 Gent, Belgium

[11] Center for Research in Agricultural Genomics, CRAG (CSIC-IRTA-UAB-UB), Campus UAB, Bellaterra, Cerdanyola del Vallès, 08193 Barcelona, Spain

[12] Current: Institute for Research in Biomedicine (IRB Barcelona), Spain

[13] Biosciences Division, Oak Ridge National Laboratory, Oak Ridge, TN 37831, USA

[14] Centre for Plant Sciences, Faculty of Biological Sciences, University of Leeds, Leeds LS2 9JT, UK

[15] Current address: Plant Molecular Cell Biology, Humboldt-University of Berlin, 10115 Berlin, Germany

[16] Structural and Genomic Information Laboratory (IGS), Aix-Marseille Université, CNRS UMR 7256 (IMM FR 3479), Marseille, France

[17] Joint Genome Institute, HudsonAlpha Institute for Biotechnology, USA

[18] DOE Joint Genome Institute, Walnut Creek, CA 94598, USA

[19] Department of Botany, University of British Columbia, Vancouver BC, V6T 1Z4, Canada

[20] Department of Biology, University of Florida, Gainesville FL 32611

[21] Department of Organismal Biology, Evolutionary Biology Centre, Uppsala University, Sweden

[22] Boyce Thompson Institute, Ithaca, New York 14853, USA

[23] Department of Molecular and Cell Biology, University of California, Berkeley, CA 94720 USA

[24] University Herbarium and Department of Integrative Biology, University of California, Berkeley, CA, 94720-2465

[25] Present: Institute for Transfusion Medicine and Immunohematology, Johann-Wolfgang-Goethe University and German Red Cross Blood Service, Sandhofstraße 1, 60528 Frankfurt am Main, Germany

[26] New York Botanical Garden, Bronx, NY 10458, USA

[27] vertis Biotechnologie AG, 85354 Freising, Lise-Meitner-Str. 30, Germany

[28] Max Planck Institute of Molecular Plant Physiology, Am Muehlenberg 1, 14476 Potsdam-Golm, Germany

[29] Department of Biology, Université Laval, Québec G1V 0A6, Canada

[30] Present: Laboratoire Reproduction et Développement des Plantes, Univ Lyon, ENS de Lyon, UCB Lyon 1, CNRS, INRA, F-69342, Lyon, France

[31] Department of Biological Sciences, University of Alberta, Edmonton AB, T6G 2E9, Canada

[32] Department of Medicine, University of Alberta, Edmonton AB, T6G 2E1, Canada

[33] BGI-Shenzhen, Beishan Industrial Zone, Yantian District, Shenzhen 518083, China

[34] Shenzhen HuahanGene Life Technology Co., Ltd., Shenzhen, China

[35] Current: Institute for Human Genetics, Medical Center – University of Freiburg, Faculty of Medicine, University of Freiburg, Germany

[36] Department of Biology, Washington University, St. Louis, MO USA

[37] BIOSS Centre for Biological Signalling Studies, University of Freiburg, Schaenzlestr. 18, 79104 Freiburg, Germany

[38] URGI, INRA, Université Paris-Saclay, 78026, Versailles, France

[39] WZW, Technical University Munich, Germany

[40] Plant Genome and Systems Biology, Helmholtz Center Munich, 85764 Neuherberg, Germany

[41] Department of Plant Biology, University of Geneva, Sciences III, Geneva 4 CH-1211, Switzerland

[42] Department of Plant Biology & Pathology, Rutgers, the State University of New Jersey, New Brunswick, NJ 08901, USA

[*] Equal contribution

+ Author for correspondence: Stefan A. Rensing; e-mail: stefan.rensing@biologie.uni-marburg.de

Running Head: Physcomitrella pseudochromosomal genome

Abstract

The draft genome of the moss model, Physcomitrella patens, comprised approximately 2,000 unordered scaffolds. In order to enable analyses of genome structure and evolution we generated a chromosome-scale genome assembly using genetic linkage as well as (end) sequencing of long DNA fragments. We find that 57% of the genome comprises transposable elements (TEs), some of which may be actively transposing during the life cycle. Unlike in flowering plant genomes, gene- and TE-rich regions show an overall even distribution along the chromosomes. However, the chromosomes are mono-centric with peaks of a class of Copia elements potentially coinciding with centromeres. Gene body methylation is evident in 5.7% of the protein-coding genes, typically coinciding with low GC and low expression. Some giant virus insertions are transcriptionally active and might protect gametes from viral infection via siRNA mediated silencing. Structure-based detection methods show that the genome evolved via two rounds of whole genome duplications (WGDs), apparently common in mosses but not in liverworts and hornworts. Several hundred genes are present in colinear regions conserved since the last common ancestor of plants. These syntenic regions are enriched for functions related to plant-specific cell growth and tissue organization. The P. patens genome lacks the TE-rich pericentromeric and gene-rich distal regions typical for most flowering plant genomes. More non-seed plant genomes are needed to unravel how plant genomes evolve, and to understand whether the P. patens genome structure is typical for mosses or bryophytes.

Introduction

The original genome sequencing of the model moss P. patens (Hedw.) Bruch & Schimp. (Funariaceae) reflected its informative phylogenetic position: a very early divergence from the evolutionary path that eventually led to the flowering plants soon after the first plants conquered land ca. 500 Ma ago (Lang et al. 2010). Previous comparisons of the moss genome with those of flowering plants and green algae provided many insights into land plant evolution (Rensing et al. 2008), detailing e.g. the evolution of abiotic stress responses and phytohormone signaling. Subsequent comparative functional genomic analyses, making use of the ability of P. patens for "reverse genetics" by gene targeting, addressed questions of how gene functions evolved to enable the increasing developmental and anatomical complexity that characterizes the dominant forms of plant life on the planet [e.g. (Horst et al. 2016, Sakakibara et al. 2013)]. The initial draft sequence encompassed close to 2,000 unordered scaffolds, significantly limiting analyses of chromosomal structure and evolution, or of the conservation of gene order during land plant evolution. We now present a new assembly accurately representing the chromosomal architecture (pseudochromosomes). Much-increased acquisition of transcriptomic evidence has substantially improved the quality of gene annotation, and acquisition of high-density DNA methylation and histone mark data combined with a detailed analysis of transposable elements (TEs) explain the size and architecture of the moss genome. This study provides unprecedented insights into the genome of a haploid-dominant land plant, such as the peculiar structure and evolution of moss chromosomes, and demonstrates syntenic conservation of important plant genes throughout 500 Ma of evolution.

Results and Discussion

The moss V3 genome: Assembly and annotation

The original genome sequence (V1.2) of Physcomitrella patens (strain Gransden 2004) comprised 1,995 sequence scaffolds (Rensing et al. 2008, Zimmer et al. 2013). Here, we integrated the previous sequence data with a high-density genetic linkage map based on 3,712 SNP segregating loci in a cross between the "Gransden 2004" (Gransden) laboratory strain and the genetically divergent "Villersexel K3" (Villersexel) accession (Kamisugi et al. 2008). The resulting assembly was further improved using novel BAC/fosmid paired end sequence data (cf. supplementary material I. for details; see section data availability for novel data associated with this study). We screened the subsequent integrated assembly for sequence contamination, producing a pseudomolecule release covering 27 nuclear chromosomes with a total genetic linkage distance of 5502.6 − 5503.1 centiMorgans (cM). The 27 chromosomal pseudomolecules include 462.3 Mbp of sequence, supplemented by 351 unplaced scaffolds representing 4.9 Mbp (1%) of unintegrated sequence, totaling 90% of the 518 Mbp estimated by flow cytometry (Schween et al. 2003). The reads partitioned as mitochondrial and plastidal were assembled de novo, yielding an improved assembly and annotation of both organellar genomes (correcting e.g. the N-terminal sequence of the plastidal RuBisCO). Structural annotation used substantial new transcript evidence (additional file 3). For parameter optimization it relied on a manually curated reference gene set (Zimmer et al. 2013), yielding gene annotation version 3.1. Of 35,307 predicted protein-coding genes, 27,511 (78%) could be functionally annotated (cf. supplementary material II.; additional file 1), i.e. encode known domains and/or encode homologs of proteins in other species. In total, 20,274 (57%) genes are expressed based on RNA-seq evidence of typical developmental stages covered by the JGI gene atlas project (http://jgi.doe.gov/our-science/science-

programs/plant-genomics/plant-flagship-genomes/); the remaining genes might be expressed in as yet unrepresented stages such as mature spores or male gametes. We found 13,160 genes to be expressed in the juvenile gametophyte (Fig. 1) - the filamentous protonemata, 12,714 in the adult gametophyte - the leafy gametophores, and 14,309 in the diploid sporophytes developing from the zygote (overlap: 10,388 genes expressed in all three developmental stages).

Unusual genome structure

Transposon content and activity

De novo analyses of repeated sequences revealed that the genome is highly repetitive, with 57% of the assembly comprising TEs, tandem repeats, unclassified repeats, and segments of host genes (cf. supplementary material III.; Table S13). The vast majority of TEs are long terminal repeat (LTR) retrotransposons (RT), strongly dominated by Gypsy-type elements that contribute almost 48%, with Copia-type elements much less abundant (3.5%). Estimated relative insertion times of LTR-RTs confirm limited accumulation of Copia-type elements over prolonged evolutionary time. By contrast, two peaks of Gypsy-type elements testify to both ancient and recent periods of significant TE activity (Fig. S7). Phylogenetic inference revealed the presence of five main LTR-RT groups including three Gypsy-type (RLG1-3) and two Copia-type elements (RLC4-5; Fig. S8). Applying a molecular clock based on sequence divergence to the full length, intact LTR-RTs indicates that the latest (<1 Ma) activity of Gypsy-type elements was mostly contributed by RLG1-3 elements, preceded by the amassing of RLG2 and RLC5 copies (around 4-6 Ma, Fig. S7, S36). RLG1 thus comprises the youngest and most abundant group among intact LTR-RTs. In line with these results, analysis of TE insertion polymorphisms between Gransden and Villersexel showed that RLG1 elements are highly polymorphic, accounting for most of the detected insertion variants (Fig.

S9). Since we detect such insertions in both accessions, the decades long in vitro culture of Gransden is not likely to be the major source of transposon activity. RLG1 elements are expressed in non-stressed protonemata (Fig. S6), which is uncommon since transposon expression is usually strongly silenced in plants and is only detected in very specific tissues such as pollen, in silencing mutants or under stress situations (Martinez et al. 2012). Moreover, recent data suggests that some stresses that typically induce plant retrotransposons, such as protoplastation, inhibit RLG1 expression (Vives et al. 2016), suggesting that RLG1 may transpose during the P. patens life cycle and might play a role in its genome dynamics. The moss germinates from spores that develop into filamentous, tip-growing protonemata (comprising chloroplast-rich chloronemal and fast-growing caulonemal cells, Fig. 1). Buds develop from caulonemal cells and grow into gametophores that bear sexual organs (gametangia). Mosses are prone to endopolyploidy (Bainard et al. 2010) and older P. patens caulonema cells endoreduplicate (Schween et al. 2005). Interestingly, endoreduplicated caulonemal cells give rise to somatic sporophytes if PpBELL1 is overexpressed, thus circumventing sexual reproduction (Horst et al. 2016). De facto 2n caulonemal cells might constitute a staging ground for (potentially transmitted) somatic changes caused via transposon activity.

Unusual chromatin structure

The genomes of most flowering plants are typically composed of monocentric chromosomes, whose unique centromeres are surrounded by heterochromatic pericentromeric regions, that are repeat-rich and gene-poor relative to distal (sub-telomeric), euchromatic regions (Lamb et al. 2007) (Fig. S34). By contrast, the landscape of gene and repeat density along P. patens chromosomes is rather homogeneous, we do not detect large repeat-rich regions with relatively low gene density (Fig. 2, 3). At a finer scale, we do detect an alternation of gene-

rich and repeat-rich regions all along the chromosomes (Fig. S10). Typical plant pericentromeres are more prone to structural variation (e.g. TE insertions and deletions) compared with the remainder of chromosome arms (Li et al. 2014). Yet, analysis of P. patens chromosomes failed to identify hotspots of structural variation that could coincide with pericentromeres (Fig. S11). It should be noted, however, that the centromeres could be present at least partially in the unassembled parts of the genome. In any case, immuno-labeling of mitotic metaphase chromosomes using a pericentromere-specific antibody demonstrates that they are mono-centric (Fig. S5). Unlike in many flowering plant genomes, the P. patens chromosomes are characterized by a more uniform distribution of eu- and heterochromatin (Fig. 3, S5, S35), raising questions about the nature and location of centromeres.

Physcomitrella centromeres seem to coincide with a particular subset of Copia elements

Plant centromeres typically comprise large arrays of satellite repeats that can be punctuated by some TEs (Wang et al. 2009). However, plotting the density of tandem repeats along the P. patens chromosomes did not reveal peaks likely to reflect the position of centromeres (Fig. S11). Computational analysis of tandem repeats in a variety of genomes identified candidate centromeric repeats in P. patens, although green algae, mosses, and liverworts contain low abundances of these (Melters et al. 2013). Positioning them on the P. patens V3 assembly revealed a patchy distribution, not single peaks that could coincide with centromeres as expected for monocentric chromosomes (Fig. S5, S11). By contrast, the low abundance Copia-type elements exhibited unusually discrete density peaks, typically one per assembled chromosome, spanning hundreds of kbp (Fig. 2, Fig. S11). Each Copia density peak principally contains RLC5 elements. A similar situation has been described in the green alga Coccomyxa subellipsoidea where a single peak of a LINE-type retrotransposon, the Zepp

element, was proposed to be involved in centromeric function (Blanc et al. 2012). The RLC5 density peak regions are generally punctuated by unresolved gaps in the assembly and by fragments of other TEs (Fig. S12). Closer examination revealed that they comprise full length LTR-RTs (FL_RLC5) as well as highly similar truncated non-autonomous variants (Tr_RLC5) that lack the integrase (INT) and reverse transcriptase domains (RVT) (Fig. S13). Remarkably, all RLC5 clusters appear to be mosaics containing nested insertions of both FL_RLC5 and Tr_RLC5 elements, of which additional copies are rare in the genome. A neutral explanation for the distribution of RLC5 clusters is that their target sequences are present at a single location per chromosome, perhaps caused by a preference for self-insertion. Alternatively, a single cluster combining FL_RLC5 and Tr_RLC5 copies may be necessary for normal chromosome function. In either case, it is possible that RLC5 clusters might be specific components of centromeres in P. patens. The dominant RLC5 peak per chromosome, highlighting the putative centromere, is marked by a radius in Figs. 1 and 3.

Alternation of activating and repressing epigenetic marks

For the V1.2 scaffolds that harbor histone 3 (H3) ChIP-seq evidence (Widiez et al. 2014), 96% can be mapped to the 27 V3 pseudochromosomes (Fig. 4); the remaining 4% map to the unassigned V3 scaffolds, underscoring the quality of the assembly. The alternating structure of genes and TE/DNA methylation (purple in Fig. 4) over the full length of the chromosomes is mirrored by activating H3 marks (K4me3, K27Ac, K9Ac; green in Fig. 4) corresponding to transcribed genic areas, and repressive H3 marks (K27me3, K9me2; red in Fig. 4) coinciding with TEs/intergenic areas. This contrasts sharply with many flowering plant genomes (Fig. S34) in which gene-rich chromosome arms display less heterochromatin than pericentromeres. Similar to flowering plant genomes, TE bodies are generally depleted for histone marks, excepting the silencing mark H3K9me2 that is above background levels in the

filamentous protonemata, and at background level in unstressed and stressed leafy gametophores (additional file 2). The previously described (Widiez et al. 2014) deposition of H3K27me3 at developmental genes that takes place with the switch from protonema to gametophore (Fig. 1) can be observed genome-wide (additional file 2). All TE bodies are methylated in similar fashion, with CG and CHG more abundant than CHH (>80% CG and CHG, >40% CHH; Fig. S15, S25-28), whereas gene bodies remain barely methylated (Fig. S15, S25-29). RLC4 has the sharpest boundary pattern (additional file 2), with almost no methylation outside the TE, followed by RLC5 with more outside-TE methylation, especially CHH. RLG1 follows in a similar fashion - although the relatively sharp pattern of RLG1 and RLC5 can in part be attributed to the fact that in case of nested insertions no "outside" TE region is present next to the TE boundary. RLG2 shows a broad pattern of all three contexts, RLG3 shows the broadest pattern with no discernible body peak. Since the methylation pattern of the main TE categories differs in how sharply they define the TE proper, TE families might have different impacts on the proximal epigenome.

Gene body methylation marks low GC genes

Interestingly, intron-containing genes (Fig. S25) show a much sharper methylation contrast between gene body and surrounding DNA, and a more pronounced difference between CHH and the other contexts, than intron-less genes (Fig. S26). As the latter genes might in part be retrocopies (Kaessmann 2010), they might be more prone to silencing and be embedded in more homogeneously methylated areas. Gene-body methylation (GBM) is found in many eukaryotic lineages and is thought to have been present in the last common eukaryotic ancestor (Feng et al. 2010). GBM in flowering plants is characterized by CG methylation of the coding sequence, not extending to transcriptional start and stop (Niederhuth et al. 2016). Such genes are typically constitutively expressed and evolutionarily conserved; however, the

functional relevance of GBM in flowering plants remains unclear (Zilberman 2017). The low incidence of genic methylation in P. patens, although all DNA methyltransferase classes are present (Dangwal et al. 2014), probably reflects secondary reduction. Despite the generally low genic methylation, 2,012 (5.7%) protein-coding genes contain at least one methylated position in gametophores (Fig. S29), and 1,155 (3.3%) of the genes show more than 50% of methylatable positions to be methylated (Fig. S30), making them GBM candidates. Most methylated genes are not expressed in gametophores (1,608 genes, 79.9%), suggesting that, contrary to flowering plants, GBM might silence them. They are also significantly less often annotated (21.7% of methylated genes carry GO terms, vs. 48.7% of all genes; $p < 0.01$, Chi-square). CHH-type methylation is most abundant (1,409 genes), followed by CHG (1,306) and CG (1,162); one third of the genes share methylation in all three contexts. The presence of CG methylation in P. patens gene bodies is in contrast to a previous report (Bewick et al. 2017), potentially due to different coverage or filtering applied. Surprisingly, given that cytosines are methylated, the average GC content of GBM genes (36.5%) is significantly ($p < 0.01$, T-test) lower than the genome-wide GC (45.9%). Genes without expression evidence in gametohores have lower GC content and GBM than those that are weakly expressed (Table S18, RPKM 0-2), while confidently expressed genes (RPKM >2) are more GC-rich and less methylated. In summary, in contrast to flowering plants low GC genes with no conserved function are principally more often found to be targeted (silenced) by DNA methylation, suggesting their potential conditional activation. GO bias analysis of the methylated genes expressed in gametophores shows enrichment of genes involved in protein phosphorylation (Fig. 31B). Most (290, 59%) of the expressed methylated genes are expressed in protonema, gametophores and green sporophytes (Fig. S31C), but 12.5% are expressed in two tissues each, while 17 (3.5%) are exlusively expressed in protonemata, 28 (5.7%) in gametophores and 93 (19%) in green sporophytes.

Do giant virus remnants guard gametes?

We mapped the genomic segments that were likely acquired horizontally from nucleocytoplasmic large DNA virus relatives [NCLDV, (Maumus et al. 2014), Table S16, Fig. 4, S14-22] and found that 87 integrations (NCLDVI) harbor 257 regions homologous to NCLDV protein-coding genes and 163 sRNA clusters. Colinearity and molecular dating analyses of NCLDVIs (Fig. S19-20) suggest four groups of regions that have been either amplified by recombination events or represent simultaneous integrations. The timing of these integrations (comprising both relatively young and older insertions/duplications) appears independent from the periods of LTR-RT activity. NCLDVI regions are the most variable annotated loci in terms of nucleotide diversity (Fig. S18). Previous evidence suggested that NCLDVI represent non-functional, decaying remnants of ancestral infections that are transcriptionally inactivated by methylation (Maumus et al. 2014). By screening available sRNA-seq libraries we could record repetitive, but specific sRNA clusters for these loci. Strikingly, we identified two NCLDV genes harboring sRNA loci that exhibit high transcriptional activity, coinciding with lower levels of DNA methylation as compared to other NCLDVI (Fig. S14, S15). Consistent with the predicted potential to form hairpin structures, sRNA Northern blots (Fig. S22) of wild type and Dicer-like (DCL) deletion mutants (Khraiwesh et al. 2010) suggest that RNA transcribed from these loci might be processed by distinct DCL proteins to generate siRNAs. These siRNAs in turn might act to target viral mRNA during a potential NCLDV infection, or to guide DNA methylation to silence these regions (Kawashima et al. 2014). Regions harboring corresponding antisense sRNA loci are enriched for stop-codon-free (i.e. non-degrading) NCLDV genes and deviate from the remainder of NCLDVI in terms of cytosine vs. histone modifications (Fig. S15, S16). Based on the similarity with intact LTR-RTs in terms of methylation and low GC (Fig. S17), and the absence of H3K9me2, we hypothesize that (like intact TEs) these ancient,

retained NCLDVi are euchromatic. We propose that they are demethylated during gametogenesis by DEMETER (which in Arabidopsis preferentially targets small, AT-rich, and nucleosome-depleted euchromatic TEs (Ibarra et al. 2012)). Given the proposed time point of activation of these regions during gametangiogenesis, NCLDVIs might provide a means to provide large numbers of siRNAs which, besides ensuring the transgenerational persistence of silencing, could also provide protection against cytoplasmatically replicating viruses via RNAi and methylation of the viral genome. This would provide efficient protection for moss gametes which, due to their dependency on water, might be the most exposed to NCLDV infections. This hypothesis provides a plausible answer to the question why endogenous NCLDV relatives have only been found in embryophytes with motile sperm cells (Maumus et al. 2014).

Genetic variability

Sequencing three different accessions we find 264,782 SNPs (1 per 1,783 bp) for Reute (collected close to Freiburg, Germany), 2,497,294 (1 per 188 bp) for Villersexel (Haute-Saône, France) and 732,288 (1 per 644p) for Kaskaskia (IL, USA) as compared to Gransden. There are 42,490 polymorphisms shared among all three accessions relative to Gransden, with other SNPs present in only one or two of the accessions (Fig. S31). SNP densities of Arabidopsis thaliana ecotypes occur at one SNP per 149 - 285 bp (Cao et al. 2011), similar to that in Villersexel, which is surprising given that the rate of neutral mutation fixation is lower in P. patens (Rensing et al. 2007). However, Villersexel has an extraordinarily high divergence compared with other P. patens accessions (McDaniel et al. 2010). Due to the fact that all accessions are inter-fertile, yet genetically divergent (Beike et al. 2014), and exhibit phenotypic differences (additional file 2)(Hiss et al. 2017), we consider them potential ecotypes. For all accessions, most SNPs (>80%) are found in intergenic and adjacent

(potential regulatory) regions of genes (Table S19). Less than 5% of all SNPs are found in genic regions, of those 34% - 36% are silent (synonymous), 62% - 64% missense (non-synonymous) and 1.6% cause a nonsense mutation. Overall, Reute shows 72 regions of SNP accumulation, whereas Villersexel and Kaskaskia show 30 and 32, respectively (Table S20-S22). The SNP accumulation hotspots in Reute are more gene-rich with 18 genes/hotspot compared with 8 and 10 in Villersexel and Kaskaskia. One peak on chromosome 16 is found in all accessions and contains genes involved in sterol catabolism and chloroplast light sensing/movement (Fig. S33). Sterols have been implicated in cell proliferation, in regulating membrane fluidity and permeability, and in modulating the activity of membrane-bound enzymes (Hartmann 1998). The over-represented terms detected in the genes commonly harboring SNPs might be the signature of evolutionary modification of dehydration tolerance, for which membrane stability has been shown to be an important factor in mosses (Hu et al. 2016, Oliver et al. 2004).

Recombination might be needed for purging TEs

Many genomes have higher densities of TEs in centromeres, sub-telomeres (Fig. S34), and sex chromosomes, i.e. regions of low recombination (Dolgin et al. 2008). One potential explanation for this biased distribution is that TEs insert with more or less equal frequencies across the genome, but are heterogeneously distributed because purifying selection is weaker in regions of low recombination. This hypothesis can be put to test using the Physcomitrella genome: the species is mostly selfing (it practises de facto asexual reproduction using sexual gametes, (Perroud et al. 2011)), and thus the effective rate of recombination is low (since genetic variants are seldom mixed as heterozygotes), and purifying selection is correspondingly weak (Szovenyi et al. 2013). If recombination (in outcrossed offspring) is indeed critical for making purifying selection effective at purging weakly deleterious TEs, we

would predict that selection against TE disruption of gene expression may be playing an important role in the chromosomal distribution of TEs (Wright et al. 2003). Hence, the unusual chromosomal structure might be a function of predominant inbreeding. We expect that the genomes of bryophytes that are outcrossers, like Marchantia polymorpha, Ceratodon purpureus, Funaria hygrometrica or Sphagnum magellanicum, might show a more biased distribution of TEs along their chromosomes.

Genome evolution

Two whole genome duplication events

Based on synonymous substitution rates (Ks) of paralogs, at least one WGD event was evident in P. patens (Rensing et al. 2007, Rensing et al. 2008). However, gene family trees often show nested paralog pairs, and the ancestral moss karyotype is hypothesized to be seven (Rensing et al. 2012) - while the extant chromosome number of P. patens is n = 27 (Reski et al. 1994), suggesting two ancestral WGD events (Rensing et al. 2012, Rensing et al. 2007). Using the novel pseudochromosome structure, Ks-based analyses support two WGDs dating back to 27-35 and 40-48 Ma (Fig. 5), respectively (cf. supplementary material IV.). Given the detected synteny, the most parsimonious explanation for the extant chromosome number is the duplication of seven ancestral chromosomes in WGD1, followed by one chromosomal loss and one fusion event during the subsequent haploidization. In WGD2 the 12 chromosomes would have duplicated again, followed by five breaks and two fusions, leading to 27 modern chromosomes. The Ks values of the above-mentioned structure-based peaks (Fig. 5) fall approximately between 0.5-0.65 (younger WGD2) and 0.75-0.9 (older WGD1). The structural and Ks information can be used to trace those genes that were present in the ancestral (pre-WGD) karyotype and have since been retained (Fig. S37, additional file 3). In total, 484 genes can be traced to the pre-WGD1 karyotype (denoted ancestor 7), and

3,112 genes to the pre-WGD2 karyotype (ancestor 12). GO bias analysis of the ancestor 7 genes shows over-representation of many genes involved in regulation of transcription and metabolism (Fig. S38). This accords with previous evidence that metabolic genes were preferentially retained after the P. patens WGD (Rensing et al. 2007), and with the trend that genes involved in transcriptional regulation are preferentially retained after plant WGDs (De Bodt et al. 2005).

WGDs are common in mosses, but not in other bryophytes

Detecting WGD events using paranome-based Ks distributions is notoriously difficult (Vanneste et al. 2014, Vekemans et al. 2012). Here we compared several methods for deconvolution of such distributions and found that a mixture model based on log-transformed values was able to detect four potential WGDs (Fig. S39), including the two that we observed based on the pseudochromosomal structure (Fig. 5). By excluding very young/low and very old/high Ks ranges, we restricted the data to the two structure-based events. Using low bandwidth (smoothing) we find that such methodology is able to detect relatively young WGDs with a clear signature (Fig. S39 E/F), whereas overlapping distributions (here the older WGD1) are hinted at via significant changes in the distribution curve at higher bandwidth settings (Fig. S39 I/J; cf. methods and supplementary material IV. / 2. for details). We applied this paranome-based WGD prediction to transcriptome data obtained from the onekp project (www.onekp.com) on 41 moss, 7 hornwort and 28 liverwort datasets and overlaid them with a molecular clock tree (Fig. S40-42) (Newton et al. 2006). For 24 of the moss samples at least one WGD signature was supported. For four out of these 24 moss datasets, mixture model components were merged into one WGD signature with the possibility of additional hidden WGD signatures. Among these species is Physcomitrium sp. which is a close relative of P. patens; shared WGD events are in accordance with previous

studies (Beike et al. 2014). The three Sphagnum species show overlap and significant gradient change support for a young WGD event and in Sphagnum lescurii also significant support for an older WGD event, supporting a recent report (Devos et al. 2016). While only a chromosome-scale assembly would be able to detect WGD events with high confidence, we note that evidence of WGDs is not detected in any of the liverwort and hornwort datasets, while the majority of moss lineages appear to have been subject to ancient WGDs. In contrast to mosses (Rensing et al. 2012, Szovenyi et al. 2014), most liverworts and hornworts are known for low levels of neo- and endopolyploidy with rather constant chromosome numbers within each lineage (Bainard et al. 2013). The three-fold fluctuations in genome size in nested hornwort lineages without a chromosomal change (Bainard et al. 2013) is thus most likely due to variable TE content. The karyotype evolution of P. patens can thus be considered as typical for moss genomes, but probably different from the genomes of hornworts and liverworts. While we do not know why mosses might be more prone to fixation of genome duplications than other bryophytes, the associated paralog acquisition and retention might be a foundation for the relative species richness of mosses (Rensing 2014, Rensing et al. 2016, Van de Peer et al. 2017).

Ancient colinearity reveals conserved plant-specific functions

Have gene orders been conserved since the last common ancestor of land plants (LAP)? Colinearity analyses with 30 other plant genomes (cf. methods and supplementary material IV. / 3.) revealed 180 colinear regions, harbouring around 1,700 genes. P. patens chromosomes contain $0.5 - 10$ of these genes per Mbp (Fig. S43), most chromosomes hence containing a number of syntenic genes that follows random expectation. Chromosomes 1, 8, 11, 14, 16 and 27, however, contain significantly more ancient colinear genes than expected ($q < 0.05$, Fisher's exact test) (additional file 3). GO bias analyses reveal that chromosome 8

is enriched for genes encoding functions for plant cell and tissue growth and development (Fig. S44). Surprisingly, several hundred genes are present in colinear regions that involve 5 to 21 other species. Moreover, 17 of these regions showed elevated levels of gene co-expression ($p < 0.05$, permutation statistics, additional file 3), indicating potential co-regulation of neighboring genes, thus corroborating the existence of conserved plant regulons (Van de Velde et al. 2016) or genomic regions exposed similarly to the transcriptional machinery. GO bias analyses of these ancient syntenic genes demonstrate that they are involved in land plant-specific cell growth and tissue organization (Fig. S45), akin to chromosome 8. Apparently, genes encoded in the LAP genome that enabled the distinct cell and tissue organization of land plants have been retained as colinear blocks throughout land plant evolution. 10 genes on chromosome 7 can be traced back to chromosome 4 of ancestor 12 (pre-WGD2), and to chromosome 2 of ancestor 7 (pre-WGD1). GO bias of chromosome 7 (Fig. S46) further supports the notion that genes enabling plant-specific development have been conserved since the LAP.

Conclusions

Our analyses show that the genome of the model moss is organized differently from seed plant genomes. In particular, no central TE-rich and distal gene-rich chromosomal areas are detected, and centromeres are potentially marked by a subclass of Copia elements. There is evidence for activation of TE and viral elements during the life cycle of P. patens that might be related to its haploid-dominant life style and motile gametes. Surprisingly, syntenic blocks harboring genes involved in plant-specific cell organization were conserved for ca. 500 Ma of land plant evolution. Chromosome-scale assemblies of other non-seed plants will be needed in order to understand how plant genomes from diverse lineages evolve, and to determine

whether the genomes of haploid-dominant plants are generally different from those of seed plants.

Materials and Methods

Sequencing and assembly

We sequenced Physcomitrella patens Gransden 2004 using a whole genome shotgun sequencing strategy. The majority of the sequencing reads were collected with standard Sanger sequencing protocols on ABI 3730XL capillary sequencing machines at the Department of Energy Joint Genome Institute in Walnut Creek, California, USA (http://www.jgi.doe.gov/sequencing/protocols/prots_production.html) as previously reported (Rensing et al. 2008). BAC end sequences were collected using standard protocols at the HudsonAlpha Institute in Huntsville, Alabama, USA. The sequencing (see Table S1) consisted of two libraries of 3Kb pairs (4.01x), 3 libraries of 8 Kb pairs (4.58x), four fosmid libraries (0.43x), and two BAC libraries (0.22x) on the Sanger platform for a total of 9.25x Sanger based coverage. A total of 7,572,652 sequence reads (9.25x assembled sequence coverage, see Table S1 for library size summary) were assembled using our modified version of Arachne v.20071016 (Jaffe et al. 2003) with parameters correct1_passes=0 maxcliq1=140 BINGE_AND_PURGE=True max_bad_look=2000 (see Table S2 for overall scaffold and contigs statistics). This produced a raw assembly consisting of 1,469 scaffolds (4,485 contigs) totaling 475.8 Mb of sequence, with a scaffold N50 of 2.8 Mb, 271 scaffolds larger than 100 kb (464.3 Mb). Scaffolds were screened against bacterial proteins, organellar sequences and the GenBank "nr" database, and removed if found to be a contaminant. Additional scaffolds were removed if they were (a) scaffolds smaller than 50kb consisting of >95% 24mers that occurred 4 other times in scaffolds larger than 50kb, (b) contained only

unanchored RNA sequences, (c) were less than 1kb in length, or (d) contaminated. Post screening, we integrated the resulting sequence with the genetic map reported here (3,712 markers), and BAC/fosmid paired end link support. An additional map (9,080 markers) was developed for chromosome 16 that resolved ordering problems present in the original map, and was used for the integration of chromosome 16. The integrated assembly was screened for contamination to produce a pseudomolecule reference covering 27 nuclear chromosomes. The pseudomolecules include 462.3 Mb of base pairs, an additional 351 unplaced scaffolds consist of 4.9 Mb of unanchored sequence. The total release includes 467.1 Mb of sequence assembled into 3,077 contigs with a contig N50 of 464.9 kbp and an N content of 1.5%. Chromosome numbers were assigned according to the physical length of each linkage group (1 = largest and 27 = smallest).

Genetic mapping

In order to assign the sequenced scaffolds representing the release version V1.2 Physcomitrella genome sequence to chromosomes, we used a genetic mapping approach based on high-density SNP markers. SNP loci between the Gransden 2004 ("Gd") and genetically divergent Villersexel K3 ("Vx") genotype were identified by Illumina sequencing (100-base paired-end reads; Illumina GAII) of the Vx accession. The sequence data have been deposited in the NCBI Sequence Read Archive as accessions SRX037761 (2 Illumina Genome Analyzer II runs: 176.1M spots, 26.8G bases, 93.4Gb downloads) and SRX030894 (3 Illumina Genome Analyzer II runs: 277.9M spots, 42.2G bases, 56Gb downloads). SNPs for linkage mapping were selected for the construction of an Illumina Infinium bead array for the GoldenGate genotyping platform, based on their distribution across the 1,921 scaffolds representing the V1.2 genome sequence assembly, with an average physical distance between SNP loci of ca. 110kbp. Segregants of a mapping population (539 progeny from Gd x Vx

crosses: (Kamisugi et al. 2008)) were genotyped at 5,542 loci to construct a linkage map using JoinMap 4.0. (Van Ooijen JW, 2006, Kyazma B.V., Wageningen, Netherlands), with a minimum independence LOD threshold of 22, a recombination threshold of 0.4, a ripple value of 1, a jump threshold of 5 and Haldane's mapping function. Of the 5,542 SNPs, 4,220 loci were represented in the final map. The map contained 27 linkage groups, covering 5,432.9 cM. Map lengths were calculated using two methods: one in which L (total map length) = Σ [(linkage group length) + 2.(linkage group length/no. markers)] (Fishman et al. 2001) and one in which L = Σ[(linkage group length.(no. markers + 1)/(no. markers -1)] (Chakravarti et al. 1991). The map corresponded to 467,985,895 bp distributed across the previously predicted 27 P. patens chromosome (Table S3). Chromosome numbers were assigned according to the overall physical length of each linkage group (1 = largest and 27 = smallest).

Pseudochromosome construction

The combination of the existing genetic map (4,220 markers), and BAC/fosmid paired end link support was used to identify 12 misjoins in the overall assembly. Misjoins were identified as linkage group discontiguity coincident with an area of low BAC/fosmid coverage. A total of 12 breaks were executed, and a total of 295 scaffolds were oriented, ordered and joined using 268 joins to form the final assembly containing 27 pseudomolecule chromosomes, capturing 462.3 Mb (98.97%) of the assembled sequence. Each chromosome join is padded with 10,000 Ns. The final assembly contains 378 scaffolds (3,077 contigs) that cover 467.1 Mb of the genome with a contig L50 of 464.9 kb and a scaffold L50 of 17.4 Mb. Completeness of the euchromatic portion of the genome assembly was assessed using 35,940 full length cDNAs. The aim of this analysis was to obtain a measure of completeness of the assembly, rather than a comprehensive examination of gene space. The cDNAs were aligned to the assembly using BLAT (Kent 2002); Parameters: -t=dna –q=rna –extendThroughN, and

alignments ≥90% base pair identity and ≥85% coverage were retained. The screened alignments indicate that 34,984 (97.3%) of the FLcDNAs aligned to the assembly. The ESTs that failed to align were checked against the NCBI nucleotide repository (nr), and a large fraction was found to be prokaryotic in origin. Significant telomeric sequence was identified using the TTTAGGG repeat, and care was taken to make sure that it was properly oriented in the production assembly. Plots of the marker placements for the 27 chromosomes are shown in additional file 2. For contamination screening, further assessment of assembly accuracy and organellar genomes please refer to supplementary material, section I.

Mapping of the v1.6 genome annotation

Gene models of the v1.6 annotation (Zimmer et al. 2013) were mapped against the V3 assembly using GenomeThreader (Gremme et al. 2005) and resulting spliced alignments were filtered and classified for consistency with the original gene structures. 93.9% of the 38,357 v1.6 transcripts could be mapped with unaltered gene structure. This comprised 29,371 loci (91.4% of the v1.6 loci). The majority of the unmappable v1.6 models represented previously unidentified bacterial or human contaminations in the V1 assembly (492 loci). Nevertheless, 49 loci with expression evidences remained unmappable in the current assembly. The mapped annotation is made available via the cosmoss.org genome browser and under the download section.

Generation of the v3.1 genome annotation

All available RNA-seq libraries (additional file 3, Table S10) were mapped to the V3 assembly using TopHat (Trapnell et al. 2009). Based on a manually curated set of cosmoss.org reference genes (Zimmer et al. 2013), libraries and resulting splice junctions were filtered to enrich evidence from mature mRNAs. Sanger and 454 EST evidences used in

the generation of the v1.6 annotation was mapped using GenomeThreader. The resulting splice junctions and exonic features were used as extrinsinc evidences to train several gene finders, which were evaluated using the cosmoss.org reference gene set. Based on this evaluation, five predictive models derived with EuGene (Foissac et al. 2003) resulting from different parameter combinations, including the original model used to predict v1.6, were retained for genome-wide predictions. RNA-seq libraries were assembled into virtual transcripts using Trinity (Grabherr et al. 2011). The resulting 1,702,106 assembled transcripts with a mean length of 1,219 bp were polyA trimmed using seqclean (part of the PASA software), of which 96% could be mapped against the V3 genome using GenomeThreader. Together with the 454 and Sanger ESTs 2,755,148 transcript sequences were used as partial cDNA evidence in the PASA software to derive 266,051 assemblies falling in 68,382 subclusters. For these, transdecoder was trained and employed to call open reading frames based on PFAM (Finn et al. 2016) domain evidence. Gene models from transdecoder, EuGene and the JGI V3.0 predictions were combined and evaluated using the eval software (Keibler et al. 2003) on the reference gene set. Based on the resulting gene and exon sensitivity and specificity scores a rank-based weight was inferred (Table S9), which was used to infer combined CDS models using EVidenceModeler, resulting in a gene sensitivity/specificity of 0.76/0.76 and an exon sensitivity/specificity of 0.93/0.98. For these combined CDS features, UTR regions were annotated using PASA in six iterations. All transcript evidences and alternative gene models are available via tracks in the cosmoss.org genome browser. From the resulting set of gene models, protein-coding gene loci and representative isoforms were inferred using a custom R script implementing a multiple feature weighting scheme that employed information about CDS orientation, proteomic, sequence similarity and expression evidence support, feature overlaps, contained repeats, UTR-introns and UTR lengths of the gene models in a Machine Learning-guided approach.

This approach was optimized and trained based on a manually curated training set in order to ideally select the functional, evolutionary conserved "major" isoform for each protein-coding gene locus. The v3.1 annotation comprises only the "major" (indicated by the isoform index 1 in the CGI), while v3.3 also includes other splice variants with isoform indices >1.

Availability of gene models and additional data

The analyses in this publication rely on the structural annotation v3.1. Subsequently, this release was merged with the phytozome-generated release v3.2, leading to the current release v3.3 which is available from http://cosmoss.org and https://phytozome.jgi.doe.gov/. Both v3.1 and v3.3 are available in CoGe (https://genomevolution.org/coge/GenomeView.pl?gid=33928), and v1.6 and v1.2 can be loaded as tracks for backward compatibility. Available experiment tracks can be downloaded and are listed in Table S12. For gene annotation version 3.2/3.3, locus naming, non-protein coding genes and functional annotation refer to supplementary material, section II. Annotation v3.1 and v3.3 are available in additional file 1, including a lookup of gene names for versions 3.3, 3.1, 1.6, 1.2 and 1.1.

Cytological analyses

The chromosome arrangement during mitotic metaphase as well as the punctate labelling at pericentromeric regions after immunolabelling with a pericentromere-specific antibody against H3S28ph (Gernand et al. 2003) indicate a monocentric chromosome structure in P. patens (Fig. S5). Furthermore, many plant genomes, as for example A. thaliana (Fuchs et al 2007), are organized in well-defined heterochromatic pericentromeric regions, decorated with typical heterochromatic marks (H3K9me1, H3K27me1) and gene-rich regions presenting the typical euchromatic marks (H3K4me2). By contrast, immunostaining experiments with

antibodies against these marks label the entire chromatin of flow-sorted interphase P. patens nuclei homogeneously (Fig. 3B). Obviously, nuclei of P. patens are thus characterized by a uniform distribution of eu- and heterochromatin.

Transposon and repeat detection and annotation

TRharvest (Ellinghaus et al. 2008) which scans the genome for LTR-RT specific structural hallmarks (like long terminal repeats, tRNA cognate primer binding sites and target site duplications) was used to identify full length LTR-RTs. The input sequences comprised the 27 pseudochromosomes plus all genomic scaffolds with a length of >=10kb together with a non redundant set of 183 P. patens tRNAs, identified beforehand via tRNA scan (Lowe et al. 1997). The used parameter settings of LTRharvest were: "overlaps best -seed 30 -minlenltr 100 -maxlenltr 2000 -mindistltr 3000 -maxdistltr 25000 -similar 85 -mintsd 4 -maxtsd 20 -motif tgca -motifmis 1 -vic 60 -xdrop 5 -mat 2 -mis -2 -ins -3 -del -3". All of the resulting 9.290 candidate sequences were annotated for PfamA domains with hmmer3 [http://hmmer.org/] and stringently filtered for false positives by several criteria, the main ones being the presence of at least one typical retrotransposon domain (e.g. RT, RH, INT, GAG) and a tandem repeat content below 25%. The filtering steps led to a final set of 2.785 high confident full-length LTR RTs. Transposons were annotated by RepeatMasker (Smit et al. 1996) against a custom-built repeat library (Spannagl et al. 2016) which included P. patens specific full length LTR-retrotransposons.

Repetitive elements have also been annotated de novo with the REPET package (v2.2). The TEdenovo pipeline from REPET (Flutre et al. 2011) was launched on the contigs of size > 350kb in the v3 assembly (representing approx. 310 Mb, gaps excluded) to build a library of consensus sequences representative of repetitive elements. Consensus sequences were built if at least five similar hits were detected in the sub-genome. Each consensus was classified with

PASTEC (Hoede et al. 2014) followed by semi-manual curation. The library was used for a first genome annotation with the TEannot pipeline (Quesneville et al. 2005) from REPET to select the consensus sequences that are present for at least one full length copy (n=349). Each selected consensus was then used to perform final genome annotation with TEannot with default settings (BLASTER sensitivity set to 2). The REPET annotations absent from the mipsREdat annotation were added to the latter to build the final repeat annotation. Tandem repeats Finder (Benson 1999) was launched with the following suite of parameters: 2 7 7 80 10 50 2000. The putative centromeric repeat previously identified through tandem repeats analysis (Melters et al. 2013) was compared to the whole V3 assembly using RepeatMasker (Smit et al. 1996) with default settings (filter divergence < 20%). Besides Copy and Gypsy-type elements (see main text), other types of TEs, including LINEs and Class II (DNA transposon) elements, appear at very low frequency (0.1% each). Simple sequence repeats represent only 2% of the assembly. For TE phylogenetic, age and expression analyses as well as NCLDV analyses refer to supplementary material, section III.

ChIP-seq data

Published CHIP-seq data (Widiez et al. 2014) for P. patens were re-analysed by mapping read libraries against the P. patens V3.0 genome sequence. Briefly, the FASTA and QUAL files were converted into FASTQ data files, which were aligned against the P. patens v3.0 genome using BWA v0.5.9 (Li et al. 2010), employing a seed length of 25, allowing a maximum of 2 mismatches on the seed and a total maximum of 10 mismatches between the reference and the reads. In order to avoid redundancy problems, all reads that were mapped to more than one genomic locus were omitted as already applied elsewhere (Stroud et al. 2012, Zemach et al. 2010). SAM files were converted into BED files using an in-house python script.

Identification of histone-modified enriched regions

For the identification of the histone-modified enriched regions (peaks) the software MACS2 v2.0.10 (Feng et al. 2012, Zhang et al. 2008) with parameters tuned for histone modification data was used. The parameters used were "no model", shift size set as "sonication fragment size", "no lambda", "broad", bandwidth 300 following the developer's instructions, fold change between 5 and 50 and q-value 0.01. As control for the peak identification the combination of Input-DNA and Mock-IP of the corresponding tissues was used as in (Widiez et al. 2014). The number of identified peaks per tissue and histone mark is shown in Table S17.

Extension of unannotated genomic regions

For several gene models in the P. patens v3.1 genome annotation the prediction of UTR regions (either 5' or 3') failed. In total there are 9,769 genes lacking the 5'-UTR and 11,385 genes lacking the 3'-UTR. Additionally, gene promoters are also unannotated. Using an approach already used in (Widiez et al. 2014), UTRs and promoters were assigned to gene models. In brief, a python script was implemented that takes as input any valid GFF3 file and (i) creates UTR regions of 300bp for genes lacking either one or both of them, (ii) creates potential promoter regions of 1,500bp upstream and downstream of each gene in the file. In the case that the space between the gene and the next element is not wide enough for the extension of the gene model by 300bp, the new UTR region is shrunken to the available space. In the case that two consecutive genes have to be extended and the space between them is less than 2x300bp the new UTRs are assigned half the space between the two genes. For the assignment of promoters the same rules apply. In no case is an element created that overlaps with existing elements of the annotation file used as input.

Filtering for expressed genes

Based on all the available JGI gene atlas (http://jgi.doe.gov/our-science/science-programs/plant-genomics/plant-flagship-genomes/) RNA-seq data downloaded from Phytozome (additional file 3), we filtered for genes that had a certain minimal RPKM value in at least one condition. At RPKM 2, 20,274 genes are expressed, at RPKM 4 18,281 genes. The RPKM cutoff of four was based on quantitative real time PCR (qRT-PCR) results of a recent microarray transcriptome atlas study (Ortiz-Ramirez et al. 2015), in which genes with this expression level were reliably detected by qPCR.

BS-seq data: Plant material and culture conditions

P. patens accession Gransden was grown in 9-cm Petri dishes on 0.9 % Agar solidified minimal (Knop's) medium. Cultures were grown under the following experimental conditions: 16 h/8 h light/dark cycle, 70 µmol sec^{-1} m^{-2}, for six weeks at 22/19°C day/night temperature following 8 h/16 h light/dark cycle, 20 µmol sec^{-1} m^{-2}, for seven weeks at 16/16 °C day/night temperature. Adult gametophores were harvested after 13 weeks and DNA was isolated according to (Dellaporta et al. 1983) with minor modifications.

Bisulfite conversion, library preparation and sequencing

Bisulfite conversion and library preparation was conducted by BGI-Shenzen, Shenzen, China according to the following procedure: DNA was fragmented to 100-300 bp by sonication, followed by blunt end DNA repair adding 3'-end dA overhang and adapter ligation. The ZYMO EZ DNA Methylation-Gold kit was used for bisulfite conversion and after desalting and size selection a PCR amplification step was conducted. After an additional size selection step the qualified library was sequenced by an Illumina GAII instrument according to manufacturer instructions resulting in 66,1086,45 paired end reads of 90bp length.

Processing of BS-seq reads

Trimmomatic v0.32 (Bolger et al. 2014) was used to clean adapter sequences, to trim and to quality-filter the reads using the following options: ILLUMINACLIP:TruSeq3-PE-2.fa:2:30:10 SLIDINGWINDOW:4:5 TRAILING:3 MINLEN:35 resulting in cleaned paired-end and orphan single-end reads. Further, the paired-end and single-end reads were mapped with Bismark v0.14 (Krueger et al. 2011) against P. patens chloroplast (NC_005087.1) and mitochondrion (NC_007945.1) sequences using the --non_directional option due to the nature of the library. After mapping the remaining single- and paired-end reads with Bismark v0.14 separately against the genome of P. patens both SAM alignment files were sorted and merged with samtools v0.1.19 (Li et al. 2009) and deduplicated with the deduplicate_bismark program of Bismark v0.14. To call methylation levels for the different cytosine contexts (CG, CHG, CHH), deduplicated SAM files and the R package methylkit (Akalin et al. 2012) were used, only considering sites with a coverage of at least nine reads and a minimal mapping quality of 20.

Gene- and TE-body methylation

Gene- and TE-body methylation levels were calculated for individual cytosine contexts (CG, CHG, CHH). For each gene and TE, all annotated feature regions (promoter, 5'-UTR, CDS, intron, 3'-UTR, TE-fragment) were combined and divided into 10 quartiles. For each quartile the mean methylation level (CG, CHG, CHH) was calculated and the average, 5% and 95% distribution per quartile and feature type were plotted. For the TE-body methylation plots TEs were further subdivided into TE-groups. For gene body methylation (GBM) analysis positions were filtered according to >=90% of the reads showing methylation. Distribution of affected genes over the three different contexts was analysed with Venny (Fig. S29; http://bioinfogp.cnb.csic.es/tools/venny/) and visualized via a stacked column diagram (Fig.

S30). Genes were grouped by RPKM value (0;>0<2;>=2) and compared with regard to GC and methylation content (Table S18).

Read mapping and variant calling

Genomic DNA sequencing data for P. patens accessions Reute (SRP068341), Villersexel (SRX030894) and Kaskaskia (SRP091316) are available from the NCBI Sequence Read Archive (SRA). The libraries were trimmed for adapters and quality filtered using trimmomatic v32 (Bolger et al. 2014) applying the following parameters: -phred33 ILLUMINACLIP:TruSeq3-PE-2.fa:2:30:8:5 SLIDINGWINDOW:4:15 TRAILING:15 MINLEN:35. After trimming, the single- and paired-end reads were initially mapped to the chloroplast genome (NC_005087.1), the mitochondrial genome (NC_007945.1) and ribosomal DNAs (HM751653.1, X80986.1, X98013.1) using GSNAP v2014-10-22 (Wu et al. 2016) with default parameters. The remaining unmapped single- and paired-end reads were used for reference mapping using GSNAP with default parameters and both resulting SAM alignment files were sorted and merged with samtools v0.1.19 (Li et al. 2009). Duplicated reads were further removed with rmdup from samtools to account for potential PCR artifacts. GATK tools v3.3.0 (McKenna et al. 2010) were used for SNP calling as recommended by the Broad institute for species without a reference SNP database including the "ploidy 1" option for the first and second haplotype calling step.

SNP validation

Called SNPs of the accession Villersexel were validated by comparing them to the Illumina Infinium bead array dataset (additional file 3) used for map construction (see map construction method section). The 4,650 bead array probes were mapped to the genome using GSNAP (Wu et al. 2016) and SNPs were called using mpileup and bcftools. In total, 4,628

SNPs could be unequivocally mapped, out of those 4,466 (96%) were also called as SNPs in the gDNA-seq based Villersexel GSNAP/GATK dataset. Thus, the vast majority of SNPs called based on deep sequence data could be independently confirmed (additional file 3).

SNP divergence estimates

To obtain window-wise (100kbp non-overlapping windows) nucleotide diversity pi and Tajima's D values, a 'pseudogenome' was constructed for each accession using a custom python script. In brief, based on the VCF file output generated by GATK all given variants were reduced to SNPs and InDels and for each accession (Kaskaskia, Reute and Villersexel) the corresponding reference sequence was substituted with the ALT allele at the given positions. These 'pseudogenome' FASTA files were additionally masked for all sites which had a read coverage < 5 which might lead to erroneous SNP calling. The masked 'pseudogenome' FASTA files were further converted into PHYLIP format and used as input for Variscan v2.0 (Hutter et al. 2006), settings "RunMode = 12", "Sliding Window = 1; WidthSW = 100000; JumpSW = 100000; WindowType = 0" and excluding alignment gaps via "CompleteDeletion = 1" (Fig. S32).

SNP hotspot detection

Window-wise (50 kbp with 10 kbp overlap) SNP numbers were extracted from the 'pseudogenome' FASTA files by a custom R script. The R functions fisher.test and p.adjust (method = "hochberg") were used to select fragments that show a significantly (adjusted p-value < 0.01) higher SNP number than the chromosome average. A SNP hotspot was called if at least five adjacent fragments showed a significantly higher SNP number (Table S20-22, Fig. S33).

Structure-based ancestral genome reconstruction and associated karyotype evolutionary model

The P. patens genome was self-aligned to identify duplicated gene pairs following the methodology previously described (Salse et al. 2009). Briefly, gene pairs are identified based on blastp alignment using CIP (cumulative identity percentage) and CALP (cumulative alignment length percentage) filtering parameters with respectively 50% and 50%. Ks (rate of synonymous substitutions) distribution of the identified pairs unveiled two peaks illuminating two WGDs, one older and one more recent, included between Ks 0.75-0.9 (WGD1) and 0.5-0.65 (WGD2).

We performed a classical dating procedure of the two WGD events based on the observed sequence divergence, taking into account the Ks ranges between 0.75-0.9 and 0.5-0.65 and a mean substitution rate (r) of 9.4×10^{-9} substitutions per synonymous site per year (Rensing et al. 2007). The time (T) since gene insertion is thus estimated using the formula $T = Ks/2r$.

Mapping of the identified gene pairs on the P. patens chromosomes defines 7 independent (non-overlapping) groups (or CARs for Contiguous Ancestral Regions) of four duplicated regions (representing two rounds of WGDs), Fig. S37. Based on the 7 CARs identified, we determined the most likely evolutionary scenario based on the assumption that the proposed evolutionary history involves the smallest number of shuffling operations (including inversions, deletions, fusions, fissions, translocations) that could account for the transition from the reconstructed ancestral genome to modern karyotype (Salse 2012). The ancestor 7 and 12 genes were mapped to the extant chromosomes and visualized as circular plots (Fig. S37). These two ancestors (7 and 12) correspond respectively to the pre-WGD1 ancestor (quadruplicated by WGD1 and WGD2 in the modern P. patens genome), and the pre-WGD2 ancestor that is the result of the duplication of ancestor7 (leading to ancestor14) after 1 fusion and 1 chromosome loss (duplicated by WGD2 in the modern P. patens genome).

Paranome-based WGD prediction

For species samples and Ks distribution calculation refer to supplementary material, section IV. We employed mixture modeling to find WGD signatures using the mclust v5.1 R package to fit a mixture model of Gaussian distributions to the raw Ks and log-transformed Ks distributions. All Ks values ≤ 0.1 were excluded for analysis to avoid the incorporation of allelic and/or splice variants and to prevent the fitting of a component to infinity (Schlueter et al. 2004, Vanneste et al. 2015), while Ks values > 5.0 were removed because of Ks saturation. Further, only WGD signatures were evaluated between the Ks range of 0.235 (12.5 MYA) to account for recently duplicated gene pairs to Ks of 2.0 to account for misleading mixture modeling above this upper limit (Vanneste et al. 2014, Vanneste et al. 2015). Because model selection criteria used to identify the optimal number of components in the mixture model are prone to over fitting (Olsen et al. 2016, Vekemans et al. 2012) we also used SiZer and SiCon (Barker et al. 2008, Chaudhuri et al. 1999) as implemented in the feature v1.2.13 R package to distinguish components corresponding to WGD features at a bandwidth of 0.0188, 0.047, 0.094 and 0.188 (corresponding 1MYA, 2.5 MYA, 5 MYA and 10 MYA) and a significance level of 0.05.

Deconvolution of the overlapping distributions that can be derived from paranome-based Ks values without structural information shows that using mixture model estimation based on log-transformed Ks values mimics structure-based WGD predictions better than using raw Ks values, resulting however in the prediction of four WGD signatures (pbSIG1: 0.15-0.32; pbSIG2: 0.48-0.60; pbSIG3: 0.7-1.12; pbSIG4: 1.66-3.45; Fig. S39 A/B). Since WGD signature prediction based on paranome-based Ks values can be misleading and is prone to over prediction (Olsen et al. 2016, Schlueter et al. 2004, Vanneste et al. 2015, Vekemans et al. 2012) we only considered Ks distribution peaks in a range of 0.235 to 2.0 as possible WGD signatures, thus excluding young paralogs potentially derived from tandem or

segmental duplication and those for which accurate dating cannot be achieved due to high age. The paranome-based WGD signatures pbSIG2 (25-32 Ma) overlaps with the younger WGD2, and pbSIG3 (37-60 Ma) overlaps with the older WGD1. Further testing for significant gradient changes in the Ks distribution applying different bandwidths showed that only pbSIG2 is detected as a significant WGD signature (significance level 0.05; Fig. S39 H), whereas pbSIG3 overlaps with a significant change of the Ks distribution curve at a bandwidth of 0.047 but shows no significant gradient change. These results show that even if one paranome-based WGD signature can be found which perfectly overlaps with a structure-based WGD signature (WGD1 and pbSIG3) it is still hard to significantly distinguish it from the younger WGD signatures (WGD2 and pbSIG2) which tend to collapse using higher bandwidths (Fig. S39 I/J). Showing that log-transformed Ks value mixture modeling at least can predict young WGD signatures and can pin point older WGD signatures we applied paranome-based WGD prediction to transcriptome data obtained from the onekp project (www.onekp.com) on 41 moss samples, 7 hornwort samples and 28 liverwort samples and overlaid them with an existing time tree (Fig. S40-S42). After evaluating the overlap of significant gradient changes on mixture model components, for 24 out of 41 moss samples at least one WGD signature was supported. For four out of these 24 moss samples mixture model components were merged into one WGD signature with the possibility of additional hidden WGD signatures. Among these samples is Physcomitrium sp. which belongs like P. patens to the Funariaceae with WGD signatures 3 (0.43-0.66) and 4 (0.80-1.07), overlapping with pbSIG2 and pbSIG3 from P. patens and hinting at WGD events in Physcomitrium 23-35 Ma and 43-57 Ma ago, respectively. For all liverwort samples and almost all hornwort samples no single predicted WGD signature was supported by three different bandwidth kernel densities. For one hornwort, namely Megaceros flagellaris, one WGD signature was supported by a significant gradient change (significance level 0.05), which disappeared using

a more stringent significance level of 0.01 and represents more likely a mixture model artifact than a true WGD signature.

Colinearity analyses

For set of species refer to supplementary material, section IV. Initially, all chromosomes from all species were compared against each other and significant colinear regions are identified. To detect colinearity within and between species i-ADHoRe 3.0 was used (Proost et al. 2012) with the following settings: alignment_method gg2, gap_size 30, cluster_gap 35, tandem gap 30, q_value 0.85, prob_cutoff 0.01, multiple_hypothesis_correection FDR, anchor_points 5 and level_2_only false. P. patens v3.1 genes were assigned to PLAZA 3.0 gene families based on the family information for the best BLASTP match (27,895 genes were assigned to 10,153 gene families). The profile-based search approach of i-ADHoRe combines the gene content information of multiple homologous genomic regions and therefore allows detection of highly degenerated though significant genomic homology (Simillion et al., 2004). In total, 180 regions were found showing significant colinearity with genomes from flowering plants (colinearity with green algal genomes was not found), comprising 1717 genes involved in syntenic regions, representing 660 unique conserved moss genes. Whereas 94/180 of the ultra-conserved colinear (UCC) regions showed genomic homology with one other species, 45 UCC regions showed colinearity with 5 or more other plant genomes. One UCC region (multiplicon 1,440, additional file 3) grouped 27 genomic segments from 21 species showing colinearity, while 70% of the UCC regions contained 5 or more conserved moss genes. Starting from the V1 moss genome assembly, only 11/180 UCC regions were recovered, demonstrating that the superior assembly V3 significantly improves the detection of ancient genomic homology. Mapping of the 660 UCC genes reveals their chromosomal location (Fig. S43). Co-expression analysis of neighboring UCC genes was performed using the Pearson

Correlation Coefficient (PCC) on the JGI gene atlas data (additional file 3) and permutation statistics were used to identify UCC regions showing significant levels of gene co-expression (i.e. based on 1,000 iterations, in how many cases was the expected median PCC for n randomly selected genes larger than the observed median PCC for n UCC genes).

We tested whether the actual number of genes detected to be present in ancient colinear blocks deviated from the expected number, if all genes were randomly distributed on the chromosomes. Chromosomes significantly deviating (Fisher's exact test and false discovery rate correction) are mentioned in the main text and are shown in additional file 3 and Fig. S43. Genes detected to be derived from ancestor 7 and ancestor 12 karyotpyes can be traced to extant chromosomes (additional file 3).

GO bias analyses and GO word cloud presentation

Analyses were conducted as described previously (Widiez et al. 2014), using the GOstats R package and Fisher's exact test with fdr correction. Visualization of the GO terms was implemented using word clouds via the http://www.wordle.net application. The weight of the given terms was defined as the $-log10(q\text{-}values)$ and the colour scheme used for the visualization was red for under-represented GO terms and green for those over-represented. Terms with stronger representation, i.e. weight >4, were represented with darker colours.

Circos plots

For the integrative visualization of the individual genomic features a karyotype ideogram was created and tracks were plotted with CIRCOS v0.67-6 (Krzywinski et al. 2009). For each feature track it is highlighted in the corresponding figure legend whether feature raw counts/values were used for visualization or if chromosomes were split into smaller windows (specifying the window size in kbp and window overlaps/jumps in kbp) using the

counts/values window average for visualization. If indicated, feature counts/values window averages (cvwa) were normalized by scaling between a range of 0 and 1 per chromosome using the following equation: $normalized\ window\ average_{chr}\left(cvwa_{i_{chr}}\right) = \frac{cvwa_{i_{chr}} - cvwa_{chr_{min}}}{cvwa_{chr_{max}} - cvwa_{chr_{min}}}$.

For normalized comparison of embryophyte chromosome structure refer to supplementary material, section III; for phylostratigraphy analyses to supplementary material, section IV.

Availability of data and material

The data reported in this paper are tabulated in Methods & supplementary material, are archived at the NCBI SRA and have been made available using the comparative genomics (CoGe) environment of CyVerse (cyverse.org) via https://genomevolution.org/coge/GenomeView.pl?gid=33928. Novel data presented with this study comprise Villersexel and Kaskaskia genomic DNA (SRX037761, SRX030894, SRP091316), genomic BAC end data (KS521087 - KS697761), RNA-seq data (Table S6; additional file 3 - available from phytozome.org), CAP-capture and BS-seq data (Table S10), and Goldengate SNP bead array data (additional file 3).

Requests for materials should be addressed to stefan.rensing@biologie.uni-marburg.de.

Authors' contributions

AS, ADZ, ACC, AW, CVC, DL, FH, FMu, FMa, GB, HG, JP, JSa, JJ, JT, JM, JF, JMC, KV, KKU, LEG, LS, MH, MT, MP, MvB, NvG, OS, PR, RM, RH, SNWH, SS, SAR, SM, TW, WM, YK, YZ analysed data or performed experiments. AL, CR, DWS, ELD, FT, FWL, GW, JCVA, JG, PFP, SAR, SG, RR, RSQ, YZ contributed samples, materials or data. DSR, DG,

JSc, JSa, JT, JMC, KV, KFXM, RR, SAR supervised part of the research. ACC, DL, FMa, SAR wrote the paper with help by SG, KFXM, DWS and contributions by all authors. JSc and SAR coordinated the project.

Acknowledgements

Supporting Information Legends

Supporting information – Figure. Microsoft Word, contains supplementary materials (I. – IV.), methods and results including Table S1 – S23, Fig. S1 – S50, and references.

Supporting information - Other, file 1. Microsoft Excel, v3.1 + v3.3 annotation.

Supporting information - Other, file 2. PDF, plots of markers, TE methylation and histone modification, phenotypic differences of P. patens accessions, sRNA Northern blots.

Supporting information - Other, file 3. Microsoft Excel, synteny analyses, JGI gene atlas samples, NCLDV clusters/genes, JGI bead array SNP QC.

References

Akalin, A., Kormaksson, M., Li, S., Garrett-Bakelman, F.E., Figueroa, M.E., Melnick, A. and Mason, C.E. (2012) methylKit: a comprehensive R package for the analysis of genome-wide DNA methylation profiles. Genome Biol, **13**, R87.

Bainard, J.D. and Newmaster, S.G. (2010) Endopolyploidy in Bryophytes: Widespread in Mosses and Absent in Liverworts. J Bot, **316356**.

Bainard, J.D. and Villarreal, J.C. (2013) Genome size increases in recently diverged hornwort clades. Genome, **56**, 431-435.

Barker, M.S., Kane, N.C., Matvienko, M., Kozik, A., Michelmore, R.W., Knapp, S.J. and Rieseberg, L.H. (2008) Multiple paleopolyploidizations during the evolution of the Compositae reveal parallel patterns of duplicate gene retention after millions of years. Mol Biol Evol, **25**, 2445-2455.

Beike, A.K., von Stackelberg, M., Schallenberg-Rudinger, M., Hanke, S.T., Follo, M., Quandt, D., McDaniel, S.F., Reski, R., Tan, B.C. and Rensing, S.A. (2014) Molecular evidence for convergent evolution and allopolyploid speciation within the Physcomitrium-Physcomitrella species complex. BMC Evol Biol, **14**, 158.

Benson, G. (1999) Tandem repeats finder: a program to analyze DNA sequences. Nucleic Acids Res, **27**, 573-580.

Bewick, A.J., Niederhuth, C.E., Ji, L., Rohr, N.A., Griffin, P.T., Leebens-Mack, J. and Schmitz, R.J. (2017) The evolution of CHROMOMETHYLASES and gene body DNA methylation in plants. Genome Biol, **18**, 65.

Blanc, G., Agarkova, I., Grimwood, J., Kuo, A., Brueggeman, A., Dunigan, D.D., Gurnon, J., Ladunga, I., Lindquist, E., Lucas, S., Pangilinan, J., Proschold, T., Salamov, A., Schmutz, J., Weeks, D., Yamada, T., Lomsadze, A., Borodovsky, M., Claverie, J.M., Grigoriev, I.V. and Van Etten, J.L. (2012) The genome of the polar eukaryotic microalga Coccomyxa subellipsoidea reveals traits of cold adaptation. Genome Biol, **13**, R39.

Bolger, A.M., Lohse, M. and Usadel, B. (2014) Trimmomatic: a flexible trimmer for Illumina sequence data. Bioinformatics, **30**, 2114-2120.

Cao, J., Schneeberger, K., Ossowski, S., Gunther, T., Bender, S., Fitz, J., Koenig, D., Lanz, C., Stegle, O., Lippert, C., Wang, X., Ott, F., Muller, J., Alonso-Blanco, C., Borgwardt, K., Schmid, K.J. and Weigel, D. (2011) Whole-genome sequencing of multiple Arabidopsis thaliana populations. Nat Genet, **43**, 956-963.

Chakravarti, A., Lasher, L.K. and Reefer, J.E. (1991) A maximum likelihood method for estimating genome length using genetic linkage data. Genetics, **128**, 175-182.

Chaudhuri, P. and Marron, J.S. (1999) SiZer for exploration of structures in curves. . J Am Stat Assoc, **94**, 807-823.

Dangwal, M., Kapoor, S. and Kapoor, M. (2014) The PpCMT chromomethylase affects cell growth and interacts with the homolog of LIKE HETEROCHROMATIN PROTEIN 1 in the moss Physcomitrella patens. Plant J, **77**, 589-603.

De Bodt, S., Maere, S. and Van de Peer, Y. (2005) Genome duplication and the origin of angiosperms. Trends Ecol Evol, **20**, 591-597.

Dellaporta, S.L., Wood, J. and Hicks, J.B. (1983) A plant DNA minipreparation: Version II. . Plant Molecular Biology Reporter, **1**, 19-21.

Devos, N., Szovenyi, P., Weston, D.J., Rothfels, C.J., Johnson, M.G. and Shaw, A.J. (2016) Analyses of transcriptome sequences reveal multiple ancient large-scale duplication events in the ancestor of Sphagnopsida (Bryophyta). New Phytol, **211**, 300-318.

Dolgin, E.S. and Charlesworth, B. (2008) The effects of recombination rate on the distribution and abundance of transposable elements. Genetics, **178**, 2169-2177.

Ellinghaus, D., Kurtz, S. and Willhoeft, U. (2008) LTRharvest, an efficient and flexible software for de novo detection of LTR retrotransposons. BMC Bioinformatics, **9**, 18.

Feng, J., Liu, T., Qin, B., Zhang, Y. and Liu, X.S. (2012) Identifying ChIP-seq enrichment using MACS. Nat Protoc, **7**, 1728-1740.

Feng, S., Cokus, S.J., Zhang, X., Chen, P.Y., Bostick, M., Goll, M.G., Hetzel, J., Jain, J., Strauss, S.H., Halpern, M.E., Ukomadu, C., Sadler, K.C., Pradhan, S., Pellegrini, M. and Jacobsen, S.E. (2010) Conservation and divergence of methylation patterning in plants and animals. Proc Natl Acad Sci U S A, **107**, 8689-8694.

Finn, R.D., Coggill, P., Eberhardt, R.Y., Eddy, S.R., Mistry, J., Mitchell, A.L., Potter, S.C., Punta, M., Qureshi, M., Sangrador-Vegas, A., Salazar, G.A., Tate, J. and Bateman, A. (2016) The Pfam protein families database: towards a more sustainable future. Nucleic Acids Res, **44**, D279-285.

Fishman, L., Kelly, A.J., Morgan, E. and Willis, J.H. (2001) A genetic map in the Mimulus guttatus species complex reveals transmission ratio distortion due to heterospecific interactions. Genetics, **159**, 1701-1716.

Flutre, T., Duprat, E., Feuillet, C. and Quesneville, H. (2011) Considering transposable element diversification in de novo annotation approaches. PLoS One, **6**, e16526.

Foissac, S., Bardou, P., Moisan, A., Cros, M.J. and Schiex, T. (2003) EUGENE'HOM: A generic similarity-based gene finder using multiple homologous sequences. Nucleic Acids Res, **31**, 3742-3745.

Gernand, D., Demidov, D. and Houben, A. (2003) The temporal and spatial pattern of histone H3 phosphorylation at serine 28 and serine 10 is similar in plants but differs between mono- and polycentric chromosomes. Cytogenet Genome Res, **101**, 172-176.

Grabherr, M.G., Haas, B.J., Yassour, M., Levin, J.Z., Thompson, D.A., Amit, I., Adiconis, X., Fan, L., Raychowdhury, R., Zeng, Q., Chen, Z., Mauceli, E., Hacohen, N., Gnirke, A., Rhind, N., di Palma, F., Birren, B.W., Nusbaum, C., Lindblad-Toh, K., Friedman, N. and Regev, A. (2011) Full-length transcriptome assembly from RNA-Seq data without a reference genome. Nat Biotechnol, **29**, 644-652.

Gremme, G., Brendel, V., Sparks, M.E. and Kurtz, S. (2005) Engineering a Software Tool for Gene Structure Prediction in Higher Organisms. Information and Software Technology., **47**, 965-978.

Harrison, C.J., Roeder, A.H., Meyerowitz, E.M. and Langdale, J.A. (2009) Local Cues and Asymmetric Cell Divisions Underpin Body Plan Transitions in the Moss Physcomitrella patens. Curr Biol, **18**, 18.

Hartmann, M.A. (1998) Plant sterols and the membrane environment Trends Plant Sci, **3**, 170-175.

Hiss, M., Meyberg, R., Westermann, J., Haas, F.B., Schneider, L., Schallenberg-Rudinger, M., Ullrich, K.K. and Rensing, S.A. (2017) Sexual reproduction, sporophyte development and molecular variation in the model moss Physcomitrella patens: introducing the ecotype Reute. Plant J, **epub doi: 10.1111/tpj.13501**.

Hoede, C., Arnoux, S., Moisset, M., Chaumier, T., Inizan, O., Jamilloux, V. and Quesneville, H. (2014) PASTEC: an automatic transposable element classification tool. PLoS One, **9**, e91929.

Horst, N.A., Katz, A., Pereman, I., Decker, E.L., Ohad, N. and Reski, R. (2016) A single homeobox gene triggers phase transition, embryogenesis and asexual reproduction. Nature Plants, **2**, 15209.

Hu, R., Xiao, L., Bao, F., Li, X. and He, Y. (2016) Dehydration-responsive features of Atrichum undulatum. J Plant Res, **129**, 945-954.

Hutter, S., Vilella, A.J. and Rozas, J. (2006) Genome-wide DNA polymorphism analyses using VariScan. BMC Bioinformatics, **7**, 409.

Ibarra, C.A., Feng, X., Schoft, V.K., Hsieh, T.F., Uzawa, R., Rodrigues, J.A., Zemach, A., Chumak, N., Machlicova, A., Nishimura, T., Rojas, D., Fischer, R.L., Tamaru, H. and Zilberman, D. (2012) Active DNA demethylation in plant companion cells reinforces transposon methylation in gametes. Science, **337**, 1360-1364.

Jaffe, D.B., Butler, J., Gnerre, S., Mauceli, E., Lindblad-Toh, K., Mesirov, J.P., Zody, M.C. and Lander, E.S. (2003) Whole-genome sequence assembly for mammalian genomes: Arachne 2. Genome Res, **13**, 91-96.

Kaessmann, H. (2010) Origins, evolution, and phenotypic impact of new genes. Genome Res, **20**, 1313-1326.

Kamisugi, Y., von Stackelberg, M., Lang, D., Care, M., Reski, R., Rensing, S.A. and Cuming, A.C. (2008) A sequence-anchored genetic linkage map for the moss, Physcomitrella patens. Plant J, **56**, 855-866.

Kawashima, T. and Berger, F. (2014) Epigenetic reprogramming in plant sexual reproduction. Nat Rev Genet, **15**, 613-624.

Keibler, E. and Brent, M.R. (2003) Eval: a software package for analysis of genome annotations. BMC Bioinformatics, **4**, 50.

Kent, W.J. (2002) BLAT--the BLAST-like alignment tool. Genome Res, **12**, 656-664.

Khraiwesh, B., Arif, M.A., Seumel, G.I., Ossowski, S., Weigel, D., Reski, R. and Frank, W. (2010) Transcriptional control of gene expression by microRNAs. Cell, **140**, 111-122.

Krueger, F. and Andrews, S.R. (2011) Bismark: a flexible aligner and methylation caller for Bisulfite-Seq applications. Bioinformatics, **27**, 1571-1572.

Krzywinski, M., Schein, J., Birol, I., Connors, J., Gascoyne, R., Horsman, D., Jones, S.J. and Marra, M.A. (2009) Circos: an information aesthetic for comparative genomics. Genome Res, **19**, 1639-1645.

Lamb, J.C., Yu, W., Han, F. and Birchler, J.A. (2007) Plant chromosomes from end to end: telomeres, heterochromatin and centromeres. Curr Opin Plant Biol, **10**, 116-122.

Lang, D., Weiche, B., Timmerhaus, G., Richardt, S., Riano-Pachon, D.M., Correa, L.G., Reski, R., Mueller-Roeber, B. and Rensing, S.A. (2010) Genome-wide phylogenetic comparative analysis of plant transcriptional regulation: a timeline of loss, gain, expansion, and correlation with complexity. Genome Biol Evol, **2**, 488-503.

Li, H. and Durbin, R. (2010) Fast and accurate long-read alignment with Burrows-Wheeler transform. Bioinformatics, **26**, 589-595.

Li, H., Handsaker, B., Wysoker, A., Fennell, T., Ruan, J., Homer, N., Marth, G., Abecasis, G., Durbin, R. and Genome Project Data Processing, S. (2009) The Sequence Alignment/Map format and SAMtools. Bioinformatics, **25**, 2078-2079.

Li, Y.H., Zhou, G., Ma, J., Jiang, W., Jin, L.G., Zhang, Z., Guo, Y., Zhang, J., Sui, Y., Zheng, L., Zhang, S.S., Zuo, Q., Shi, X.H., Li, Y.F., Zhang, W.K., Hu, Y., Kong, G., Hong, H.L., Tan, B., Song, J., Liu, Z.X., Wang, Y., Ruan, H., Yeung, C.K., Liu, J., Wang, H., Zhang, L.J., Guan, R.X., Wang, K.J., Li, W.B., Chen, S.Y., Chang, R.Z., Jiang, Z., Jackson, S.A., Li, R. and Qiu, L.J. (2014) De novo assembly of soybean wild relatives for pan-genome analysis of diversity and agronomic traits. Nat Biotechnol, **32**, 1045-1052.

Lowe, T.M. and Eddy, S.R. (1997) tRNAscan-SE: a program for improved detection of transfer RNA genes in genomic sequence. Nucleic Acids Res, **25**, 955-964.

Martinez, G. and Slotkin, R.K. (2012) Developmental relaxation of transposable element silencing in plants: functional or byproduct? Curr Opin Plant Biol, **15**, 496-502.

Maumus, F., Epert, A., Nogue, F. and Blanc, G. (2014) Plant genomes enclose footprints of past infections by giant virus relatives. Nature Communications, **5**, 4268.

McDaniel, S.F., von Stackelberg, M., Richardt, S., Quatrano, R.S., Reski, R. and Rensing, S.A. (2010) The speciation history of the Physcomitrium-Physcomitrella species complex. Evolution, **64**, 217-231.

McKenna, A., Hanna, M., Banks, E., Sivachenko, A., Cibulskis, K., Kernytsky, A., Garimella, K., Altshuler, D., Gabriel, S., Daly, M. and DePristo, M.A. (2010) The Genome Analysis Toolkit: a MapReduce framework for analyzing next-generation DNA sequencing data. Genome Res, **20**, 1297-1303.

Melters, D.P., Bradnam, K.R., Young, H.A., Telis, N., May, M.R., Ruby, J.G., Sebra, R., Peluso, P., Eid, J., Rank, D., Garcia, J.F., DeRisi, J.L., Smith, T., Tobias, C.,

Ross-Ibarra, J., Korf, I. and Chan, S.W. (2013) Comparative analysis of tandem repeats from hundreds of species reveals unique insights into centromere evolution. Genome Biol, **14**, R10.

Newton, A.E., Wikström, N., Bell, N., Forrest, L.L. and Ignatov, M.S. (2006) Dating the diversification of the pleurocarpous mosses. In Pleurocarpous mosses: Systematics and Evolution (Tangney, N. ed. CRC Press, Boca Raton: Systematics Association.

Niederhuth, C.E., Bewick, A.J., Ji, L., Alabady, M.S., Kim, K.D., Li, Q., Rohr, N.A., Rambani, A., Burke, J.M., Udall, J.A., Egesi, C., Schmutz, J., Grimwood, J., Jackson, S.A., Springer, N.M. and Schmitz, R.J. (2016) Widespread natural variation of DNA methylation within angiosperms. Genome Biol, **17**, 194.

Oliver, M.J., Dowd, S.E., Zaragoza, J., Mauget, S.A. and Payton, P.R. (2004) The rehydration transcriptome of the desiccation-tolerant bryophyte Tortula ruralis: transcript classification and analysis. BMC Genomics, **5**, 89.

Olsen, J.L., Rouze, P., Verhelst, B., Lin, Y.C., Bayer, T., Collen, J., Dattolo, E., De Paoli, E., Dittami, S., Maumus, F., Michel, G., Kersting, A., Lauritano, C., Lohaus, R., Topel, M., Tonon, T., Vanneste, K., Amirebrahimi, M., Brakel, J., Bostrom, C., Chovatia, M., Grimwood, J., Jenkins, J.W., Jueterbock, A., Mraz, A., Stam, W.T., Tice, H., Bornberg-Bauer, E., Green, P.J., Pearson, G.A., Procaccini, G., Duarte, C.M., Schmutz, J., Reusch, T.B. and Van de Peer, Y. (2016) The genome of the seagrass Zostera marina reveals angiosperm adaptation to the sea. Nature, **530**, 331-335.

Ortiz-Ramirez, C., Hernandez-Coronado, M., Thamm, A., Catarino, B., Wang, M., Dolan, L., Feijo, J.A. and Becker, J.D. (2015) A transcriptome atlas of Physcomitrella patens provides insights into the evolution and development of land plants. Mol Plant, **9**, 205-220.

Perroud, P.F., Cove, D.J., Quatrano, R.S. and McDaniel, S.F. (2011) An experimental method to facilitate the identification of hybrid sporophytes in the moss Physcomitrella patens using fluorescent tagged lines. New Phytol, **2**, 1469-8137.

Proost, S., Fostier, J., De Witte, D., Dhoedt, B., Demeester, P., Van de Peer, Y. and Vandepoele, K. (2012) i-ADHoRe 3.0--fast and sensitive detection of genomic homology in extremely large data sets. Nucleic Acids Res, **40**, e11.

Quesneville, H., Bergman, C.M., Andrieu, O., Autard, D., Nouaud, D., Ashburner, M. and Anxolabehere, D. (2005) Combined evidence annotation of transposable elements in genome sequences. PLoS Comput Biol, **1**, 166-175.

Rensing, S.A. (2014) Gene duplication as a driver of plant morphogenetic evolution. Current Opinion in Plant Biology, **17C**, 43-48.

Rensing, S.A., Beike, A.K. and Lang, D. (2012) Evolutionary importance of generative polyploidy for genome evolution of haploid-dominant land plants   In Plant Genome Diversity (Greilhuber, J., Wendel, J.F., Leitch, I.J. and Doležel, J. eds). Vienna, New York: Springer.

Rensing, S.A., Ick, J., Fawcett, J.A., Lang, D., Zimmer, A., Van de Peer, Y. and Reski, R. (2007) An ancient genome duplication contributed to the abundance of metabolic genes in the moss Physcomitrella patens. BMC Evol Biol, **7**, 130.

Rensing, S.A., Lang, D., Zimmer, A.D., Terry, A., Salamov, A., Shapiro, H., Nishiyama, T., Perroud, P.-F., Lindquist, E.A., Kamisugi, Y., Tanahashi, T., Sakakibara, K., Fujita, T., Oishi, K., Shin-I, T., Kuroki, Y., Toyoda, A., Suzuki, Y., Hashimoto, S.-i., Yamaguchi, K., Sugano, S., Kohara, Y., Fujiyama, A., Anterola, A., Aoki, S., Ashton, N., Barbazuk, W.B., Barker, E., Bennetzen, J.L., Blankenship, R., Cho, S.H., Dutcher, S.K., Estelle, M., Fawcett, J.A., Gundlach, H., Hanada, K., Heyl, A., Hicks, K.A., Hughes, J., Lohr, M., Mayer, K., Melkozernov, A.,

Murata, T., Nelson, D.R., Pils, B., Prigge, M., Reiss, B., Renner, T., Rombauts, S., Rushton, P.J., Sanderfoot, A., Schween, G., Shiu, S.-H., Stueber, K., Theodoulou, F.L., Tu, H., Van de Peer, Y., Verrier, P.J., Waters, E., Wood, A., Yang, L., Cove, D., Cuming, A.C., Hasebe, M., Lucas, S., Mishler, B.D., Reski, R., Grigoriev, I.V., Quatrano, R.S. and Boore, J.L. (2008) The Physcomitrella genome reveals evolutionary insights into the conquest of land by plants. Science, **319**, 64-69.

Rensing, S.A., Sheerin, D.J. and Hiltbrunner, A. (2016) Phytochromes: More Than Meets the Eye. Trends Plant Sci, **21**, 543-546.

Reski, R., Faust, M., Wang, X.H., Wehe, M. and Abel, W.O. (1994) Genome analysis of the moss Physcomitrella patens (Hedw.) B.S.G. Mol Gen Genet, **244**, 352-359.

Sakakibara, K., Ando, S., Yip, H.K., Tamada, Y., Hiwatashi, Y., Murata, T., Deguchi, H., Hasebe, M. and Bowman, J.L. (2013) KNOX2 genes regulate the haploid-to-diploid morphological transition in land plants. Science, **339**, 1067-1070.

Salse, J. (2012) In silico archeogenomics unveils modern plant genome organisation, regulation and evolution. Curr Opin Plant Biol, **15**, 122-130.

Salse, J., Abrouk, M., Murat, F., Quraishi, U.M. and Feuillet, C. (2009) Improved criteria and comparative genomics tool provide new insights into grass paleogenomics. Brief Bioinform, **10**, 619-630.

Schlueter, J.A., Dixon, P., Granger, C., Grant, D., Clark, L., Doyle, J.J. and Shoemaker, R.C. (2004) Mining EST databases to resolve evolutionary events in major crop species. Genome, **47**, 868-876.

Schween, G., Egener, T., Fritzkowsky, D., Granado, J., Guitton, M.-C., Hartmann, N., Hohe, A., Holtorf, H., Lang, D., Lucht, J.M., Reinhard, C., Rensing, S.A., Schlink, K., Schulte, J. and Reski, R. (2005) Large-scale analysis of 73,329 gene-

disrupted Physcomitrella mutants: production parameters and mutant phenotypes. Plant Biology, **7**, 238-250.

Schween, G., Gorr, G., Hohe, A. and Reski, R. (2003) Unique tissue-specific cell cycle in Physcomitrella. Plant Biology, **5**, 50-58.

Smit, A.F.A., Hubley, R. and Green, P. (1996) RepeatMasker Open-3.0. URL http://www. repeatmasker. org.(unpublished), **2004**.

Spannagl, M., Nussbaumer, T., Bader, K.C., Martis, M.M., Seidel, M., Kugler, K.G., Gundlach, H. and Mayer, K.F. (2016) PGSB PlantsDB: updates to the database framework for comparative plant genome research. Nucleic Acids Res, **44**, D1141-1147.

Stroud, H., Otero, S., Desvoyes, B., Ramirez-Parra, E., Jacobsen, S.E. and Gutierrez, C. (2012) Genome-wide analysis of histone H3.1 and H3.3 variants in Arabidopsis thaliana. Proc Natl Acad Sci U S A, **109**, 5370-5375.

Szovenyi, P., Perroud, P.F., Symeonidi, A., Stevenson, S., Quatrano, R.S., Rensing, S.A., Cuming, A.C. and McDaniel, S.F. (2014) De novo assembly and comparative analysis of the Ceratodon purpureus transcriptome. Mol Ecol Resour.

Szovenyi, P., Ricca, M., Hock, Z., Shaw, J.A., Shimizu, K.K. and Wagner, A. (2013) Selection is no more efficient in haploid than in diploid life stages of an angiosperm and a moss. Molecular Biology and Evolution, **30**, 1929-1939.

Trapnell, C., Pachter, L. and Salzberg, S.L. (2009) TopHat: discovering splice junctions with RNA-Seq. Bioinformatics, **25**, 1105-1111.

Van de Peer, Y., Mizrachi, E. and Marchal, K. (2017) The evolutionary significance of polyploidy. Nat Rev Genet, **18**, 411-424.

Van de Velde, J., Van Bel, M., Van Eechoutte, D. and Vandepoele, K. (2016) A Collection of Conserved Non-Coding Sequences to Study Gene Regulation in Flowering Plants. Plant Physiol.

Vanneste, K., Baele, G., Maere, S. and Van de Peer, Y. (2014) Analysis of 41 plant genomes supports a wave of successful genome duplications in association with the Cretaceous-Paleogene boundary. Genome Research.

Vanneste, K., Sterck, L., Myburg, A.A., Van de Peer, Y. and Mizrachi, E. (2015) Horsetails Are Ancient Polyploids: Evidence from Equisetum giganteum. Plant Cell, **27**, 1567-1578.

Vekemans, D., Proost, S., Vanneste, K., Coenen, H., Viaene, T., Ruelens, P., Maere, S., Van de Peer, Y. and Geuten, K. (2012) Gamma paleohexaploidy in the stem lineage of core eudicots: significance for MADS-box gene and species diversification. Mol Biol Evol, **29**, 3793-3806.

Vives, C., Charlot, F., Mhiri, C., Contreras, B., Daniel, J., Epert, A., Voytas, D.F., Grandbastien, M.A., Nogue, F. and Casacuberta, J.M. (2016) Highly efficient gene tagging in the bryophyte Physcomitrella patens using the tobacco (Nicotiana tabacum) Tnt1 retrotransposon. New Phytol, **212**, 759-769.

Wang, G., Zhang, X. and Jin, W. (2009) An overview of plant centromeres. J Genet Genomics, **36**, 529-537.

Widiez, T., Symeonidi, A., Luo, C., Lam, E., Lawton, M. and Rensing, S.A. (2014) The chromatin landscape of the moss Physcomitrella patens and its dynamics during development and drought stress. Plant J, **79**, 67-81.

Wright, S.I., Agrawal, N. and Bureau, T.E. (2003) Effects of recombination rate and gene density on transposable element distributions in Arabidopsis thaliana. Genome Res, **13**, 1897-1903.

Wu, T.D., Reeder, J., Lawrence, M., Becker, G. and Brauer, M.J. (2016) GMAP and GSNAP for Genomic Sequence Alignment: Enhancements to Speed, Accuracy, and Functionality. Methods Mol Biol, **1418**, 283-334.

Zemach, A., McDaniel, I.E., Silva, P. and Zilberman, D. (2010) Genome-wide evolutionary analysis of eukaryotic DNA methylation. Science, **328**, 916-919.

Zhang, Y., Liu, T., Meyer, C.A., Eeckhoute, J., Johnson, D.S., Bernstein, B.E., Nusbaum, C., Myers, R.M., Brown, M., Li, W. and Liu, X.S. (2008) Model-based analysis of ChIP-Seq (MACS). Genome Biol, **9**, R137.

Zilberman, D. (2017) An evolutionary case for functional gene body methylation in plants and animals. Genome Biol, **18**, 87.

Zimmer, A.D., Lang, D., Buchta, K., Rombauts, S., Nishiyama, T., Hasebe, M., Van de Peer, Y., Rensing, S.A. and Reski, R. (2013) Reannotation and extended community resources for the genome of the non-seed plant Physcomitrella patens provide insights into the evolution of plant gene structures and functions. BMC Genomics, **14**, 498.

Figures Legends

Fig. 1. The P. patens life cycle.

Germination of haploid spores yields the juvenile gametophytic generation, the protonema. Protonema grows two-dimensional by apical (tip) growth and side branching. Protonemata consist of chloroplast-rich chloronema cells, and longer, thinner caulonema cells featuring less chloroplasts and oblique cross walls. Three-faced buds featuring single apical stem cells emerge from side branches (Harrison et al. 2009) to form the adult gametophytic phase, the leafy gametophores. Gametophores comprise basal, multicellular rhizoids for nutrient supply, as well as non-vascular leaves (phyllids). Gametangia (female archegonia and male antheridia) develop on the gametophores. Upon fertilization of the egg cell by motile

spermatozoids the diploid zygote forms and subsequently performs embryogenesis. Spore mother cells in the diploid sporophyte undergo meiosis to form spores.

Fig. 2. Chromosome structure, focus on TEs.

From outer to inner: karyotype bands colored according to ancestral genome blocks as in Fig. 5 (scale = Mbp), followed by 1) gene density (grey, normalized 0,1), 2) repeat density (violet, normalized 0,1), 3) Gypsy-type elements (blue, normalized 0,1), 4) Copia-type elements (blue, normalized 0,1), 5) RLC5 elements (orange, histogram). For each chromosome, a radius marks the dominant RLC5 peak, potentially coinciding with the centromere (see text). All plots are based on a 500 kbp sliding window (400 kbp jump). Chromosomes are arranged according to the ancestral (pre-WGD) seven chromosome karytope (Fig. 5).

Fig. 3. Comparative analysis of genome structures.

Comparative data of Arabidopsis thaliana (left) and Physcomitrella patens (right) reveals the lack of large heterochromatic blocks (b) that is mirrored by even distribution of recombination rate, gene and LTR-RT distribution (a) in the moss.

a) Averaged topology of genomic features based on 1,000 non-overlapping windows per chromosome (averaged over all chromosomes); arbitrary units, 1,000 representing the full length of the averaged chromosomes. Upper track: Smoothed chromosomal densities of intact LTRs, protein-coding genes and the normalized mean recombination rate. Lower track: Smoothed density curves of H3K4me3 and H3K9me2 histone modification peak regions. b) Immunostaining of typical eu- and heterochromatin-associated histone methylation marks (H3K4me2, H3K9me1 and H3K27me1) on flow-sorted interphase nuclei.

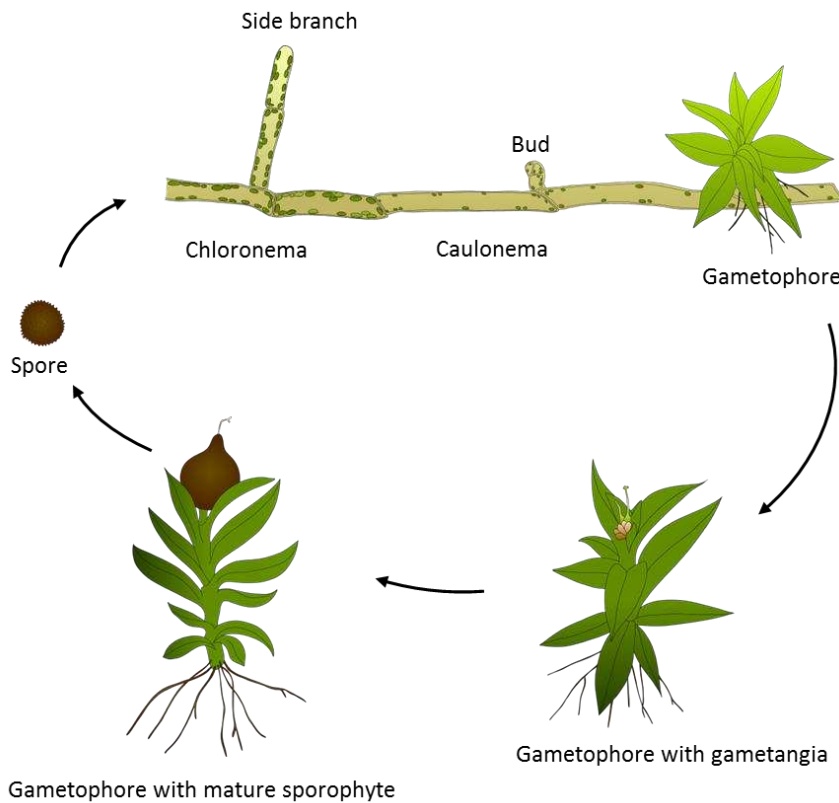**Fig. 4**: **Chromosome structure, focus on epigenetic marks.**

From outer to inner: karyotype bands colored according to ancestral genome blocks as in Fig. 5, followed by: 1) Gene density (grey) normalized 0,1; 2) GC content 0.25 - 0.45 (blue); 3) all TEs density (violet) normalized 0,1, NCLDV evidence is shown as radial orange lines; 4) methylation (red): CHH + CHG + CG, each median per window normalized 0,1, 0.0 - 3.0 (individual tracks see Fig. S32); 5) Gametophore H3 repression marks (red, K27me3, K9me2) percent per window normalized, 0.0 - 2.0 (for more detailed plots see additional file 1); 6) Protonema H3 repression marks (red, K27me3, K9me2) normalized as in 5.; 7) Gametophore H3 activation marks (green, K4me3, K27Ac, K9Ac) normalized as in 5.; 8. Protonema H3 activation marks (green, K4me3, K27Ac, K9Ac) normalized as in 5.; 9) Nucleotide diversity (blue histogram) 0.0 - 0.01. RLC5 radius as in Fig. 1. 9) 100kbp sliding window and 100kbp jump, all other plots as in Fig. 1. Chromosomes are arranged according to the ancestral (pre-WGD) seven chromosome karytope (Fig. 5).

Fig. 5. Evolutionary scenario leading to the modern P. patens genome.

A) Ks distribution (y-axis) of paralogous pairs (x-axis) inherited from two (blue for older and red for more recent) WGD events. B) Dotplot representation of the paralogous pairs belonging to two WGD events. C) Karyotype evolution of the P. patens genome from an n=7 ancestor through two WGDs. The modern P. patens genome is illustrated as a mosaic of coloured chromosomal blocks highlighting chromosome ancestry.
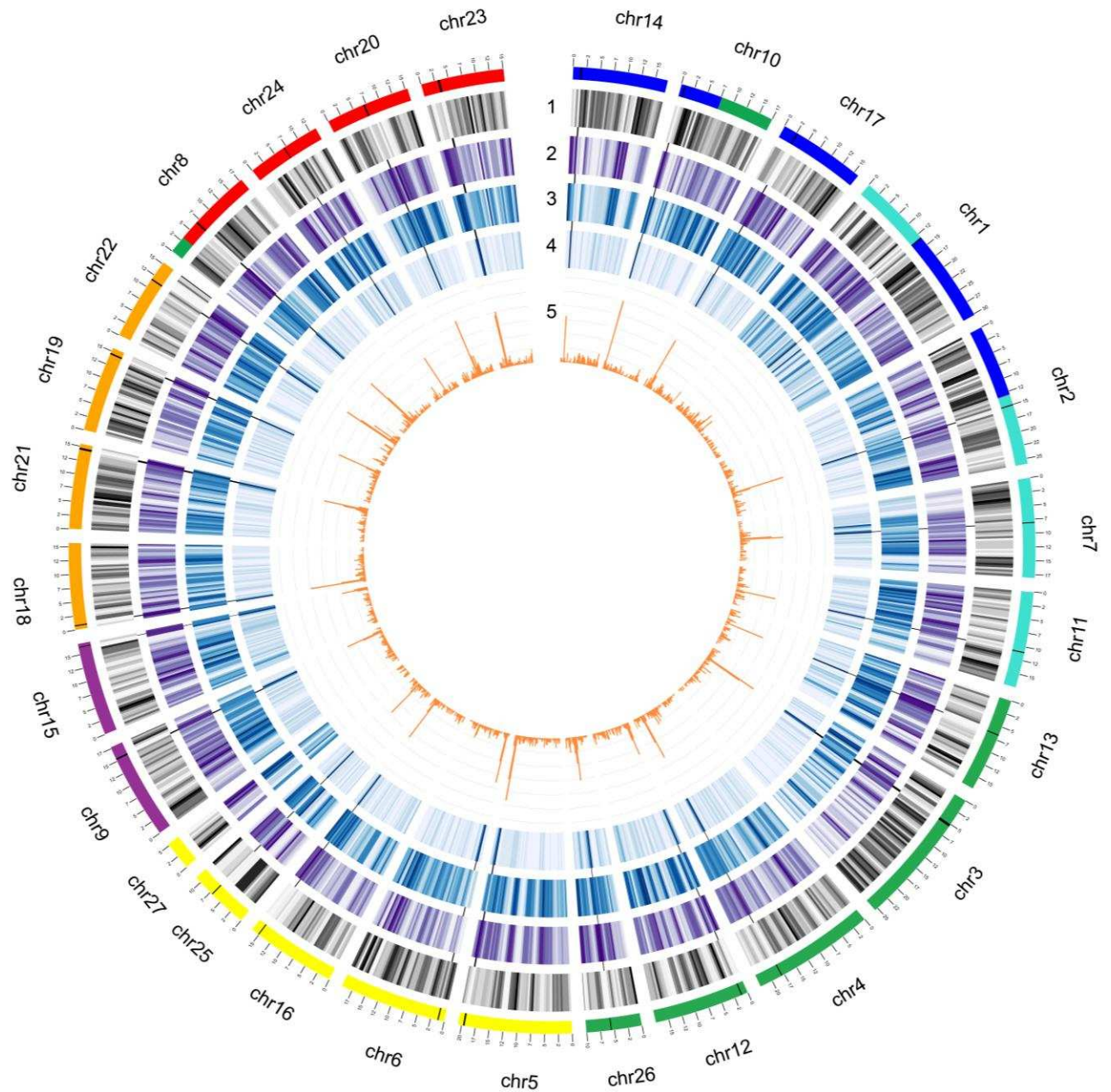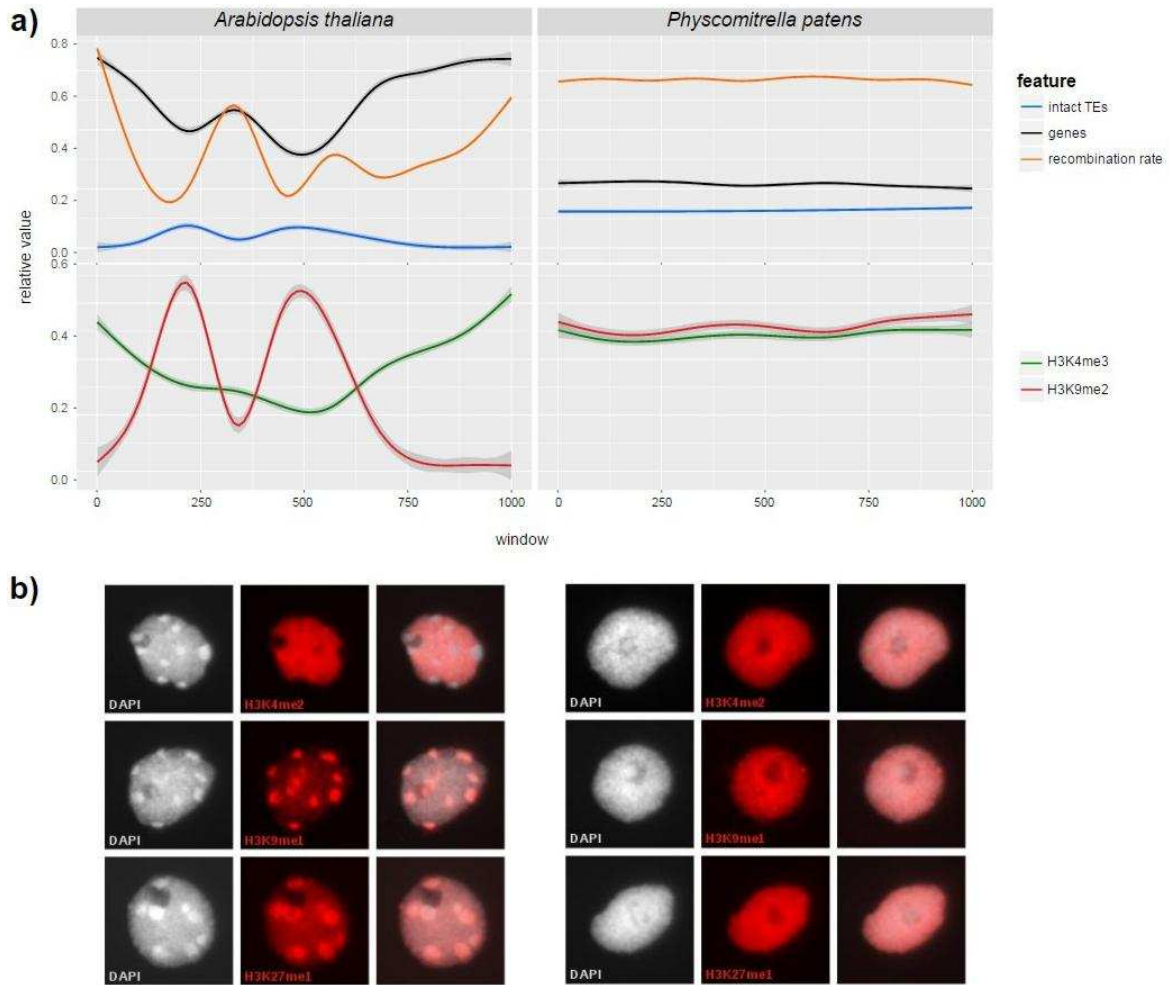
Figures

Fig. 1: **The P. patens life cycle.**

Germination of haploid spores yields the juvenile gametophytic generation, the protonema. Protonema grows two-dimensional by apical (tip) growth and side branching. Protonemata consist of chloroplast-rich chloronema cells, and longer, thinner caulonema cells featuring less chloroplasts and oblique cross walls. Three-faced buds featuring single apical stem cells emerge from side branches (Harrison et al. 2009) to form the adult gametophytic phase, the leafy gametophores. Gametophores comprise basal, multicellular rhizoids for nutrient supply, as well as non-vascular leaves (phyllids). Gametangia (female archegonia and male antheridia) develop on the gametophores. Upon fertilization of the egg cell by motile spermatozoids the diploid zygote forms and subsequently performs embryogenesis. Spore mother cells in the diploid sporophyte undergo meiosis to form spores.

Fig. 2: **Chromosome structure, focus on TEs.**

From outer to inner: karyotype bands colored according to ancestral genome blocks as in Fig. 5 (scale = Mbp), followed by 1) gene density (grey, normalized 0,1), 2) repeat density (violet, normalized 0,1), 3) Gypsy-type elements (blue, normalized 0,1), 4) Copia-type elements (blue, normalized 0,1), 5) RLC5 elements (orange, histogram). For each chromosome, a radius marks the dominant RLC5 peak, potentially coinciding with the centromere (see text). All plots are based on a 500 kbp sliding window (400 kbp jump). Chromosomes are arranged according to the ancestral (pre-WGD) seven chromosome karytope (Fig. 5).
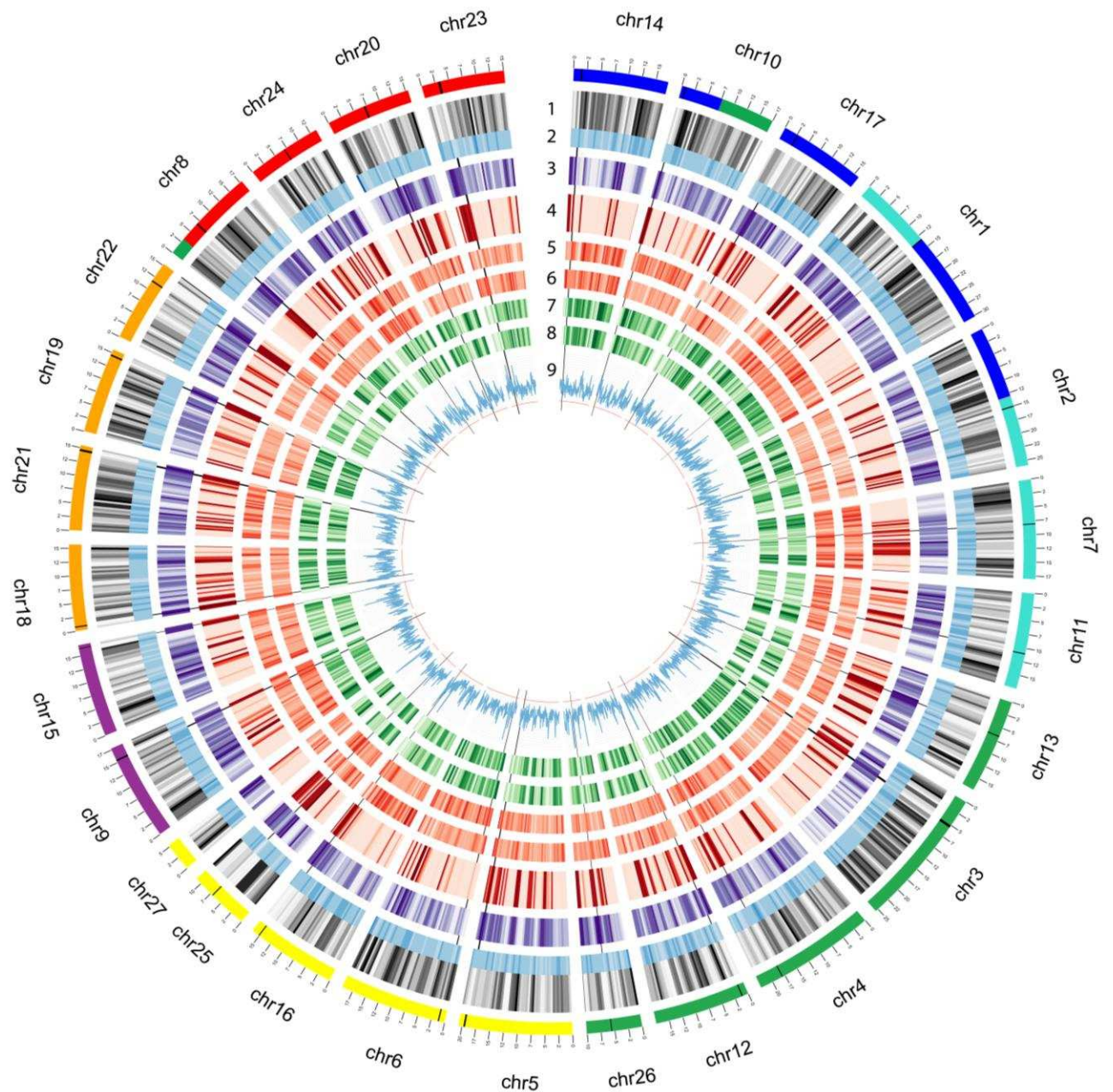
Fig. 3: **Comparative analysis of genome structures.**

Comparative data of Arabidopsis thaliana (left) and Physcomitrella patens (right) reveals the lack of large heterochromatic blocks (b) that is mirrored by even distribution of recombination rate, gene and LTR-RT distribution (a) in the moss.
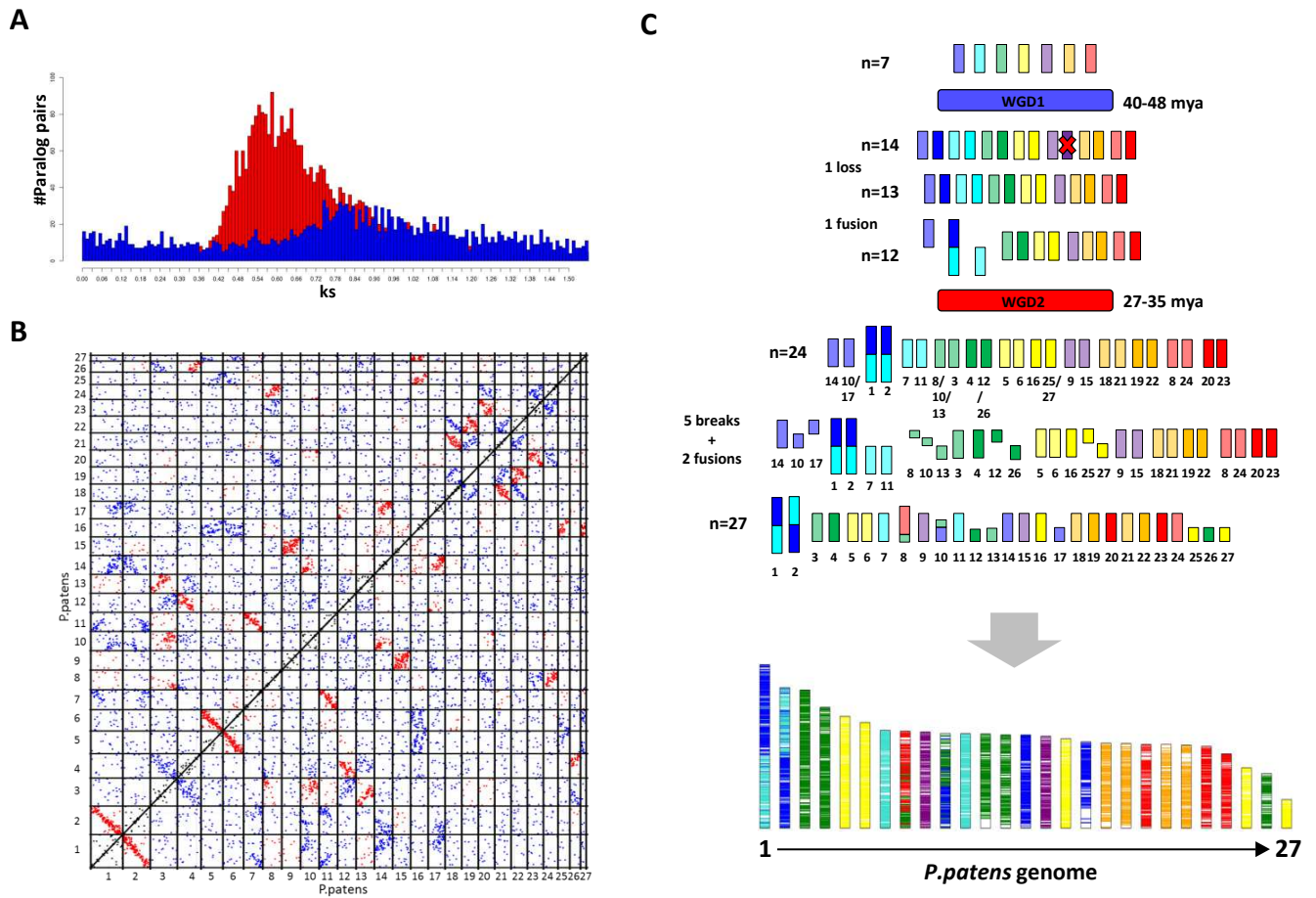
a) Averaged topology of genomic features based on 1,000 non-overlapping windows per chromosome (averaged over all chromosomes); arbitrary units, 1,000 representing the full length of the averaged chromosomes. Upper track: Smoothed chromosomal densities of intact LTRs, protein-coding genes and the normalized mean recombination rate. Lower track: Smoothed density curves of H3K4me3 and H3K9me2 histone modification peak regions. b) Immunostaining of typical eu- and heterochromatin-associated histone methylation marks (H3K4me2, H3K9me1 and H3K27me1) on flow-sorted interphase nuclei.

Fig. 4: **Chromosome structure, focus on epigenetic marks.**

From outer to inner: karyotype bands colored according to ancestral genome blocks as in Fig. 5, followed by: 1) Gene density (grey) normalized 0,1; 2) GC content 0.25 - 0.45 (blue); 3) all TEs density (violet) normalized 0,1, NCLDV evidence is shown as radial orange lines; 4) methylation (red): CHH + CHG + CG, each median per window normalized 0,1, 0.0 - 3.0 (individual tracks see Fig. S32); 5) Gametophore H3 repression marks (red, K27me3, K9me2) percent per window normalized, 0.0 - 2.0 (for more detailed plots see additional file 1); 6) Protonema H3 repression marks (red, K27me3, K9me2) normalized as in 5.; 7) Gametophore H3 activation marks (green, K4me3, K27Ac, K9Ac) normalized as in 5.; 8. Protonema H3 activation marks (green, K4me3, K27Ac, K9Ac) normalized as in 5.; 9) Nucleotide diversity (blue histogram) 0.0 - 0.01. RLC5 radius as in Fig. 1. 9) 100kbp sliding window and 100kbp jump, all other plots as in Fig. 1. Chromosomes are arranged according to the ancestral (pre-WGD) seven chromosome karytope (Fig. 5).

Fig. 5: Evolutionary scenario leading to the modern P. patens genome.

A) Ks distribution (y-axis) of paralogous pairs (x-axis) inherited from two (blue for older and red for more recent) WGD events. B) Dotplot representation of the paralogous pairs belonging to two WGD events. C) Karyotype evolution of the P. patens genome from an n=7 ancestor through two WGDs. The modern P. patens genome is illustrated as a mosaic of coloured chromosomal blocks highlighting chromosome ancestry.